Holographic Integrated Sensing and Communication

Haobo Zhang, Hongliang Zhang, Boya Di, Marco Di Renzo, Zhu Han, H. Vincent Poor, Lingyang Song

Holographic Integrated Sensing and Communication

Haobo Zhang, *Student Member, IEEE,* Hongliang Zhang, *Member, IEEE,* Boya Di, *Member, IEEE,* Marco Di Renzo, *Fellow, IEEE,* Zhu Han, *Fellow, IEEE,* H. Vincent Poor, *Life Fellow, IEEE,* and Lingyang Song, *Fellow, IEEE*

***Abstract*—To overcome spectrum congestion, a promising approach is to integrate sensing and communication (ISAC) functions in one hardware platform. Recently, metamaterial antennas, whose tunable radiation elements are arranged more densely than those of traditional multiple-input-multiple-output (MIMO) arrays, have been developed to enhance the sensing and communication performance by offering a finer controllability of the antenna beampattern. In this paper, we propose a holographic beamforming scheme, which is enabled by metamaterial antennas with tunable radiated amplitudes, that jointly performs sensing and communication. However, it is challenging to design the beamformer for ISAC functions by taking into account the unique amplitude-controlled structure of holographic beamforming. To address this challenge, we formulate an integrated sensing and communication problem to optimize the beamformer, and design a holographic beamforming optimization algorithm to efficiently solve the formulated problem. A lower bound for the maximum beampattern gain is provided through theoretical analysis, which reveals the potential performance enhancement gain that is obtained by densely deploying several elements in a metamaterial antenna. Simulation results substantiate the theoretical analysis and show that the maximum beamforming gain of a metamaterial antenna that utilizes the proposed holographic beamforming scheme can be increased by at least 50% compared with that of a traditional MIMO array of the same size. In addition, the cost of the proposed scheme is lower than that of a traditional MIMO scheme while providing the same ISAC performance.**

***Index Terms*—Holographic integrated sensing and communication, holographic beamforming, reconfigurable holographic surfaces.**

I. Introduction

With the growing demand for capacity in wireless networks, spectrum resources are becoming increasingly scarce. This asks for new paradigms and technologies to overcome the spectrum congestion in wireless systems [1], [2]. Integrated sensing and communication (ISAC) [3], [4] has been recently proposed as one approach to mitigating this problem in a way that radar sensing and communication tasks are integrated and co-designed in a single hardware platform and the spectrum of both radar and communication systems is shared [5], [6]. By carefully designing the hardware platform and the signal processing algorithms of ISAC systems, a considerable enhancement of the spectral and cost efficiency can be obtained, as compared with separate communication and radar systems operating in isolated frequency bands [7].

Based on the antenna configuration, existing ISAC systems can be categorized into two types: single-antenna and multi-antenna systems [8], [9]. Though the single-antenna configuration is easy to implement due to the low hardware complexity [10], [11], the number of spatial degrees of freedom provided by a single-antenna configuration is limited, and thus it is not able to simultaneously detect targets and serve communication users in different directions. In contrast, multi-antenna platforms with multi-beam steering capability have been introduced in [12]-[15], where the number of spatial degrees of freedom is enhanced to support simultaneous multi-target sensing and multi-user communication. In [12], the authors consider a fully digital multiple-input-multiple-output (MIMO) system that transmits radar waveforms and communication signals at the same time, and that minimizes the multi-user interference energy and the mismatch error between the desired and the transmitted radar beampatterns. In [13], the weighted sum of the beampattern matching error and the beampattern cross correlation is minimized by optimizing the digital beamformers to improve the radar performance. Also, signal-to-interference-plus-noise ratio (SINR) constraints are considered to guarantee the communication performance of the downlink users. A hybrid analog-digital (HAD) beamforming structure is employed in [14] to reduce the hardware complexity and cost of fully digital MIMO arrays.

However, the antenna spacing in MIMO arrays is usually equal to half of the wavelength due to the implementation difficulties of manufacturing antennas of sub-wavelength size and due to the mutual coupling that arises among closely spaced antennas [15], [16]. These two issues usually limit the number of antenna elements that can be deployed in an antenna-array of a given size, which results in a small antenna gain and insufficient ISAC performance [17], [18]. Recently, metamaterial antennas have been developed as a promising solution to lift the half-wavelength restrictions [19]. Due to the unique structure of the radiation elements in the metamaterial antenna, the size of the radiation elements and the spacing between nearby radiation elements can be much smaller than half of the wavelength, leading to superior beam-steering capabilities [20], [21]. One typical metamaterial antenna that

Manuscript received August 23, 2021; revised December 11, 2021; accepted January 14, 2022. This work was supported in part by the National Natural Science Foundation of China under Grants 61829101 and 61941101, in part by the European Commission through the H2020 ARIADNE project under grant agreement number 871464 and through the H2020 RISE-6G project under grant agreement number 101017011, and in part by NSF CNS-2107216, EARS-1839818 and Toyota. (Corresponding author: Lingyang Song.)

H. Zhang, B. Di, and L. Song are with Department of Electronics, Peking University, Beijing 100871, China (e-mail: {haobo.zhang,diboya,lingyang.song}@pku.edu.cn).

H. Zhang and H. Vincent Poor are with Department of Electrical and Computer Engineering, Princeton University, NJ 08544, USA (e-mail: {hz16,poor}@princeton.edu).

M. Di Renzo is with Université Paris-Saclay, CNRS, CentraleSupélec, Laboratoire des Signaux et Systèmes, 3 Rue Joliot-Curie, 91192 Gif-sur-Yvette, France. (marco.di-renzo@universite-paris-saclay.fr).

Z. Han is with the Department of Electrical and Computer Engineering in the University of Houston, Houston, TX 77004, USA, and also with the Department of Computer Science and Engineering, Kyung Hee University, Seoul, South Korea, 446-701 (e-mail: zhan2@uh.edu).

enables ultra-thin and integrated transmitter/receiver design is the reconfigurable holographic surface (RHS)[1]. It has been applied for commercial use in cellular communications [24] and satellite communications [25], showing great potential to reduce the system complexity and cost without performance degradation.

Existing works have proposed various metamaterial enabled holographic beamforming schemes for application to wireless communications [26], [27], imaging [28], and satellite applications [29]. In [26], the authors consider the downlink transmission between a base station (BS) equipped with an RHS and multiple users, and the sum rate of the communication system is maximized via holographic beamforming under a total power constraint at the BS. The authors of [28] develop a microwave imaging system which leverages holographic beamforming and computational imaging techniques for target reconstruction. A metasurface antenna which performs holographic beamforming on a satellite platform is designed in [29]. However, these schemes only consider the beam-steering capabilities for communication, imaging, or satellite applications, and thus they cannot be directly applied to ISAC systems.

In this paper, we consider a holographic beamforming enabled ISAC scenario. Specifically, holographic beamforming is performed by a BS equipped with an RHS, where the BS applies digital beamforming, and the RHS performs analog beamforming by tuning the radiated amplitude of each metamaterial element in the RHS. It is worth noting that the analog beamforming at the RHS is different from that in a traditional HAD structure which is based on the phase-shifting of the radio-frequency (RF) signals [30], [27]. Through holographic beamforming, a desired beampattern that points towards the directions of the targets and, at the same time, fulfills the SINR requirements of all the communication users can be generated by optimizing the digital and analog beamformers. By using printed-circuit-board (PCB) technologies, this technique can be implemented at a low cost. For example, the RHS and the electronic circuits that control the amplitudes of the signals emitted by the metamaterial elements of the RHS can be fabricated on PCB boards [26], [31].

Designing an optimized system based on holographic beamforming is, however, a non-trivial task due to the following two reasons. *First*, since the analog beamforming at the RHS operates in an amplitude-controlled manner, new beamforming schemes are required to fully exploit the potential benefits of holographic beamforming for ISAC. *Second*, the designs of the beamformers at the BS and the RHS are coupled with each other, which complicates the design of radar-communication beampatterns. In response to the above challenges, we advance the state-of-the-art in the following ways:

- We consider an ISAC system that consists of a BS equipped with an RHS, multiple radar targets, and multiple communication users. A holographic beamforming scheme for ISAC is designed, where the BS implements the digital beamforming and the RHS implements the amplitude-controlled analog beamforming for simultaneously detecting the radar targets and serving the downlink communication users.
- We formulate a holographic integrated sensing and communication problem where the beampattern gains towards the directions of the targets are maximized and the cross-correlation among these directions are minimized by optimizing the digital and analog beamformers. A holographic beamforming optimization algorithm is proposed to efficiently solve the formulated problem in an iterative manner.
- We investigate the performance of the proposed scheme based on holographic beamforming. Theoretical and simulation results validate the effectiveness of the proposed scheme, whose maximum beamforming gain is be increased by at least 50% compared with that of a traditional HAD-based MIMO array of the same size. Also, the cost-effectiveness is higher than that of a traditional HAD-based MIMO array.

The rest of this paper is organized as follows. In Section II, we describe the model of the ISAC system based on holographic beamforming. In Section III, the corresponding holographic beamforming scheme is proposed. The holographic integrated sensing and communication problem is formulated in Section IV, and the holographic beamforming optimization algorithm is presented in Section V. In Section VI, we analyze the performance of the proposed system. Section VII reports the simulation results, and final conclusions are drawn in Section VIII.

Notation: $(\cdot)^*$, $(\cdot)^{\mathrm{T}}$, $(\cdot)^{\mathrm{H}}$, and $(\cdot)^{-1}$ denote the conjugate, transpose, conjugate transpose, and inverse operators, respectively. $\circ$ and $\otimes$ denote the Hadamard (elementwise) product and the Kronecker product, respectively. $\mathbb{R}^{M\times N}$, $\mathbb{S}^{M\times N}$, $\mathbb{C}^{M\times N}$, and $\mathbb{H}^{M\times N}$ denote the set of all real, symmetric, complex, and Hermitian $M\times N$ matrices, respectively. $\mathbf{1}^{M\times N}$ is an $M\times N$ matrix with all the elements being 1, and $\boldsymbol{I}^{M\times N}$ is the $M\times N$ identity matrix. $\mathbb{E}(\cdot)$ denotes the expectation. $||\boldsymbol{\beta}||$ is the Euclidean norm of a vector $\boldsymbol{\beta}$. $\mathrm{tr}(\cdot)$ and $\mathrm{vec}(\cdot)$ denote the trace and vector operators, respectively. $\mathrm{Re}(\cdot)$ represents the real part of a complex variable.

II. System Model

In this section, we we first describe the ISAC system enabled by holographic beamforming in Subsection II-A, and then introduce the basic principles of RHSs in Subsection II-B.

A. Scenario Description

As shown in Fig. 1, we consider an ISAC system that consists of L mobile users denoted by $\mathcal{L}=\{1,\cdots,l,\cdots,L\}$, multiple targets, and a BS equipped with an RHS and a MIMO antenna array. To perform sensing and communication functionalities, the following three steps are executed sequentially.

- **Optimization:** The BS optimizes the ISAC signals to maximize the radar performance and to assure the target quality of service (QoS) to communication users.

[1]The structure of an RHS is much simpler than that of a MIMO array [22]. Specifically, the RHS uses compact metamaterial elements and does not require active phase shifters for beampattern reconfigurability, leading to a lower profile and a higher integration density [23].

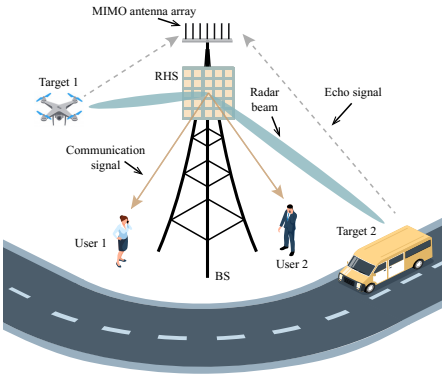

Fig. 1. A holographic integrated sensing and communication system.

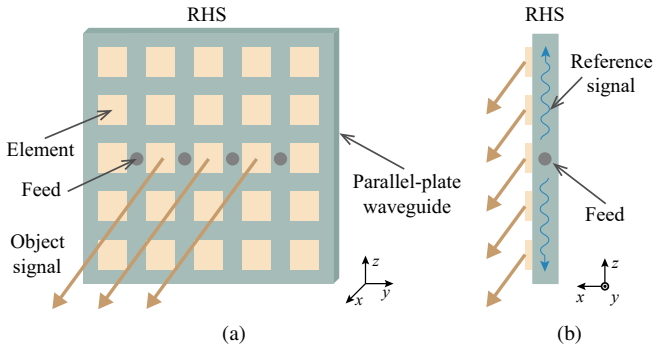

Fig. 2. Diagram of an RHS: (a) Perspective view; (b) Right view.

- **Transmission:** The RHS transmits the ISAC signals with multiple beams towards the directions of the users and targets.
- **Reception:** The communication users receive the signals from the RHS and decode the received signals to obtain the communication information. At the same time, the MIMO antenna array listens to the echo signals reflected by the targets for radar sensing[2].

In traditional MIMO systems [13], multiple beams are emitted by large antenna arrays whose elements are connected to many RF chains or phase shifters, resulting in complex structures that require costly circuits and hardware. In holographic beamforming based ISAC systems, by contrast, the beams with desired properties are generated by an RHS that is made of closely spaced radiating elements and a limited number of RF chains, which provide powerful beam-steering capabilities [34] and significantly reduce the complexity and cost [24].

B. RHS Basic Principles

An RHS is a type of planar antenna with a reconfigurable architecture that is capable of synthesizing different radiation patterns. As illustrated in Fig. 2(a), it is composed of K feeds that are connected to K RF chains, a parallel-plate waveguide, and M reconfigurable metamaterial elements whose sizes and inter-distances are usually smaller than half of the wavelength. A metamaterial element can be realized with structures like complementary-electric-resonator (CELC) and slots [30]. In contrast to a phased array that adjusts the phase shifts of the signals to generate different beampatterns, each metamaterial element of an RHS is capable of changing the amplitude of the signals to realize the desired radiation pattern.

In general, an RHS works as follows. First, the feeds embedded at the bottom of the RHS emit the signals $\boldsymbol{x} = (x_1, \cdots, x_K)^{\mathrm{T}} \in \mathbb{C}^{K\times 1}$, where x_k is the signal emitted by the k-th feed. Then, the signal emitted by each feed propagates in the waveguide. This signal is usually referred to as the *reference signal*. The reference signal at the location of the m-th metamaterial element can be expressed as[3]

$$x_m^r = \sum_{k=1}^{K} x_k \exp(-j\boldsymbol{k}_m^k(\boldsymbol{r}_m^e - \boldsymbol{r}_k^f)), \tag{1}$$

where $\boldsymbol{k}_m^k$ is the propagation vector of the reference wave emitted by the k-th feed, which is defined as

$$\boldsymbol{k}_m^k = \frac{2\pi n_r f}{v_c} \cdot \frac{(\boldsymbol{r}_m^e - \boldsymbol{r}_k^f)^{\mathrm{T}}}{|\boldsymbol{r}_m^e - \boldsymbol{r}_k^f|}, \tag{2}$$

where n_r denotes the refractive index of the substrate of the waveguide, f denotes the frequency of the reference wave, v_c denotes the speed of light, $\boldsymbol{r}_m^e$ is the location of the m-th element, and $\boldsymbol{r}_k^f$ is the location of the k-th feed. The vector $\boldsymbol{r}_k^f$ is defined as $\boldsymbol{r}_k^f = (r_k^{f,x}, r_k^{f,y}, r_k^{f,z})^{\mathrm{T}}$, where $r_k^{f,x}$, $r_k^{f,y}$, and $r_k^{f,z}$ denote the x, y, and z-coordinates of the k-th feed, respectively. The reference signal excites the metamaterial element to radiate the so-called *object signal*. Specifically, the object signal radiated by the m-th element is given by

$$x_m^o = \psi_m x_m^r, \tag{3}$$

where ψ_m is a non-negative number that represents the radiated amplitude of the m-th element, which can be selected among C^s different values denoted by $\{0, \frac{1}{C^s-1}, \cdots, 1\}$ [23]. If, for example, the radiation amplitude is quantized with N_b bits, we have $C^s = 2^{N_b}$ different amplitude values[4]. Therefore, the object signal generated through the analog beamforming can be expressed as

$$\boldsymbol{x}^o = \boldsymbol{\Psi}\boldsymbol{Q}\boldsymbol{x}, \tag{4}$$

where $\boldsymbol{\Psi} = \mathrm{diag}(\boldsymbol{\psi}) \in \mathbb{C}^{M\times M}$ denotes the analog beamforming matrix, and $\boldsymbol{\psi} = (\psi_1, \cdots, \psi_M)$ is the vector of radiated amplitudes of all the metamaterial elements of the RHS, which is referred to as the *analog beamforming vector*.

[2]Since the processing of the received echo signals can be performed by using the techniques proposed in [32], [33] when the ISAC signals are given, in this paper we focus our attention only on how to optimize the ISAC signals of the proposed system.

[3]In (1), for mathematical simplicity, we assume that the strength of the reference signal does not change when the signal propagates in the waveguide. This assumption is accurate when the size of the RHS is not large ($M < 400$ for example) because the power emitted from each element and the power loss in the wave propagation is relatively small compared to the power of the reference signal [19], [30].

[4]In practice, the number of quantization bits N_b can be chosen to lie in $[1, 8]$ [19], [34]. If $N_b = 2$, for example, the values of ψ_m belong to the set $\{0, 1/3, 2/3, 1\}$.

The matrix $\boldsymbol{Q} \in \mathbb{C}^{M\times K}$ collects the phase shifts from the feeds to the metamaterial elements, whose (m,k)-th element is $\exp(-j\boldsymbol{k}_m^k(\boldsymbol{r}_m^e - \boldsymbol{r}_k^f))$.

III. Holographic Beamforming Scheme

In this section, we first introduce the structure of the holographic beamforming scheme. Based on the proposed holographic beamforming scheme, the SINR for communication and the beampattern for radar sensing are then formulated.

A. Structure of the Holographic Beamforming Scheme

The block diagram of the considered holographic beamforming scheme is illustrated in Fig. 3. The proposed scheme consists of two parts: the digital beamforming at the BS and the analog beamforming at the RHS. The communication data streams and radar waveforms are first processed by the BS via digital beamforming and are then sent to the RHS for generating the desired ISAC signals via analog beamforming. Specifically, L data streams and K radar waveforms are first processed by the BS via the digital beamformers for communication $\boldsymbol{B}_c \in \mathbb{C}^{K\times L}$ and for radar sensing $\boldsymbol{B}_s \in \mathbb{C}^{K\times K}$, respectively. The L data streams carry the information to be sent to L different users. Besides, in order to exploit the degrees of freedom created by the K RF chains, K radar waveforms are precoded and sent to the RF chains together with the processed data streams [13]. Consequently, the signal sent to the K RF chains can be expressed as

$$\boldsymbol{x} = \boldsymbol{B}_c\boldsymbol{c} + \boldsymbol{B}_s\boldsymbol{s}, \tag{5}$$

where $\boldsymbol{c} = (c_1,\cdots,c_l,\cdots,c_L)^{\mathrm{T}} \in \mathbb{C}^{L\times 1}$ denotes the communication symbols intended to the L users, and $\boldsymbol{s} = (s_1,\cdots,s_k,\cdots,s_K)^{\mathrm{T}} \in \mathbb{C}^{K\times 1}$ denotes the radar waveforms. As shown in Fig. 3, each RF chain is connected to one of the feeds in the RHS. The signal $\boldsymbol{x}$ is input to the feeds via K RF chains, which convert it from the digital to the RF domain. Then, the signals radiated by the feeds propagate through the waveguide, and, finally, they are radiated by the amplitude-controlled radiation elements. Based on (4), the object signal generated by the holographic beamforming scheme can be written as

$$\boldsymbol{x}^o = \boldsymbol{\Psi}\boldsymbol{Q}(\boldsymbol{B}_c\boldsymbol{c} + \boldsymbol{B}_s\boldsymbol{s}). \tag{6}$$

Without loss of generality, we assume that each element of the communication symbol $\boldsymbol{c}$ and each element of the radar waveform $\boldsymbol{s}$ have unit power, which can be formulated as

$$\mathbb{E}(c_lc_l) = 1, \forall l, \tag{7}$$

$$\mathbb{E}(s_ks_k) = 1, \forall k. \tag{8}$$

Furthermore, each communication stream (or radar waveform) is uncorrelated with the other communication streams or radar waveforms [5], which can be expressed as

$$\mathbb{E}(c_lc_{l'}) = 0, \forall l, l', l \neq l', \tag{9}$$

$$\mathbb{E}(s_ks_{k'}) = 0, \forall k, k', k \neq k', \tag{10}$$

$$\mathbb{E}(c_ls_k) = 0, \forall l, k. \tag{11}$$

B. SINR Model for Communication

The SINR of each user is utilized as the performance indicator for communication tasks. Let $\boldsymbol{h}_l = (h_{l,1},\cdots,h_{l,m},\cdots,h_{l,M})$ denote the channel from the RHS to the l-th mobile user, where $h_{l,m}$ is the channel from the m-th element to the l-th mobile user. The signal received by the l-th user can be expressed as

$$\begin{aligned} y_l &= \boldsymbol{h}_l^{\mathrm{T}}\boldsymbol{\Psi}\boldsymbol{Q}(\boldsymbol{B}_c\boldsymbol{c} + \boldsymbol{B}_s\boldsymbol{s}) + v_l, \\ &= \boldsymbol{h}_l^{\mathrm{T}}\boldsymbol{\Psi}\boldsymbol{Q}\boldsymbol{b}_{c,l}c_l + \boldsymbol{h}_l^{\mathrm{T}}\boldsymbol{\Psi}\boldsymbol{Q}\sum_{l'\neq l}\boldsymbol{b}_{c,l'}c_{l'} + \boldsymbol{h}_l^{\mathrm{T}}\boldsymbol{\Psi}\boldsymbol{Q}\boldsymbol{B}_s\boldsymbol{s} + v_l, \end{aligned} \tag{12}$$

where $\boldsymbol{b}_{c,l}$ is the l-th column of matrix $\boldsymbol{B}_c$, and v_l is the noise term which is a complex Gaussian random variable, i.e., $\mathcal{CN}(0,\sigma^2)$. In (12), the second and the third terms represent the interference and the noise for the l-th user, respectively, Therefore, the SINR of the l-th user can be expressed as

$$\gamma_l = \frac{|\boldsymbol{h}_l^{\mathrm{T}}\boldsymbol{\Psi}\boldsymbol{Q}\boldsymbol{b}_{c,l}|^2}{|\boldsymbol{h}_l^{\mathrm{T}}\boldsymbol{\Psi}\boldsymbol{Q}\sum_{l'\neq l}\boldsymbol{b}_{c,l'}|^2 + \boldsymbol{h}_l^{\mathrm{T}}\boldsymbol{\Psi}\boldsymbol{Q}\boldsymbol{B}_s\boldsymbol{B}_s^{\mathrm{H}}\boldsymbol{Q}^{\mathrm{H}}\boldsymbol{\Psi}^{\mathrm{H}}\boldsymbol{h}_l^* + \sigma^2}. \tag{13}$$

Let us define $\boldsymbol{B} = (\boldsymbol{B}_c, \boldsymbol{B}_s)$, and let $\boldsymbol{b}_l$ denote the l-th column of matrix $\boldsymbol{B}$. Then, the SINR of the l-th user can be reformulated as follows

$$\gamma_l = \frac{\boldsymbol{h}_l^{\mathrm{T}}\boldsymbol{\Psi}\boldsymbol{Q}\boldsymbol{R}_l\boldsymbol{Q}^{\mathrm{H}}\boldsymbol{\Psi}^{\mathrm{H}}\boldsymbol{h}_l^*}{\boldsymbol{h}_l^{\mathrm{T}}\boldsymbol{\Psi}\boldsymbol{Q}\boldsymbol{R}\boldsymbol{Q}^{\mathrm{H}}\boldsymbol{\Psi}^{\mathrm{H}}\boldsymbol{h}_l^* - \boldsymbol{h}_l^{\mathrm{T}}\boldsymbol{\Psi}\boldsymbol{Q}\boldsymbol{R}_l\boldsymbol{Q}^{\mathrm{H}}\boldsymbol{\Psi}^{\mathrm{H}}\boldsymbol{h}_l^* + \sigma^2}, \tag{14}$$

where we have introduced the covariance matrices $\boldsymbol{R}_l = \boldsymbol{b}_l\boldsymbol{b}_l^{\mathrm{H}} \in \mathbb{C}^{K\times K}$ and $\boldsymbol{R} = \boldsymbol{B}\boldsymbol{B}^{\mathrm{H}} = \sum_{l=1}^{L+K}\boldsymbol{b}_l\boldsymbol{b}_l^{\mathrm{H}}$.

C. Beampattern Model for Radar Sensing

In this subsection, we introduce the farfield power beampattern for radar sensing. We assume that the center of the RHS is located at the origin. The farfield signal towards the direction (θ,ϕ) can be written as

$$z(\theta,\phi) = \boldsymbol{a}^{\mathrm{T}}(\theta,\phi)\boldsymbol{\Psi}\boldsymbol{Q}(\boldsymbol{B}_c\boldsymbol{c} + \boldsymbol{B}_s\boldsymbol{s}), \tag{15}$$

where $\boldsymbol{a}(\theta,\phi) = (a_1(\theta,\phi),\cdots,a_m(\theta,\phi),\cdots,a_M(\theta,\phi))^{\mathrm{T}} \in \mathbb{C}^{M\times 1}$ denotes the steering vector of the RHS, and $a_m(\theta,\phi)$ is given by

$$a_m(\theta,\phi) = \exp(-j\boldsymbol{k}_f(\theta,\phi)\boldsymbol{r}_m^e), \tag{16}$$

where $\boldsymbol{k}_f(\theta,\phi)$ is the propagation vector in free space of the object signal with direction (θ,ϕ). Therefore, the beampattern gain towards the direction (θ,ϕ) is given by

$$P(\theta,\phi) = \mathbb{E}(z(\theta,\phi)z^*(\theta,\phi)) = \boldsymbol{a}^{\mathrm{T}}(\theta,\phi)\boldsymbol{\Psi}\boldsymbol{Q}\boldsymbol{R}\boldsymbol{Q}^{\mathrm{H}}\boldsymbol{\Psi}^{\mathrm{H}}\boldsymbol{a}^*(\theta,\phi). \tag{17}$$

Furthermore, the cross-correlation between the directions (θ,ϕ) and (θ',ϕ') can be expressed as

$$\begin{aligned} P^c(\theta,\phi,\theta',\phi') &= \mathbb{E}(z(\theta,\phi)z^*(\theta',\phi')) \\ &= \boldsymbol{a}^{\mathrm{T}}(\theta,\phi)\boldsymbol{\Psi}\boldsymbol{Q}\boldsymbol{R}\boldsymbol{Q}^{\mathrm{H}}\boldsymbol{\Psi}^{\mathrm{H}}\boldsymbol{a}^*(\theta',\phi'). \end{aligned} \tag{18}$$

[5] This assumption holds in practice by properly choosing the codes for communication and radar sensing. Specifically, the uncorrelatedness of different communication streams can be assured by assigning orthogonal codes to different communication users [35]. By generating radar waveforms using pseudo random codes, in addition, that radar waveforms can be assured to be uncorrelated with other radar waveforms or with the communication streams [35], [36]. Thus, the uncorrelatedness between one communication stream (or radar waveform) and another communication stream (or radar waveform) can be guaranteed.

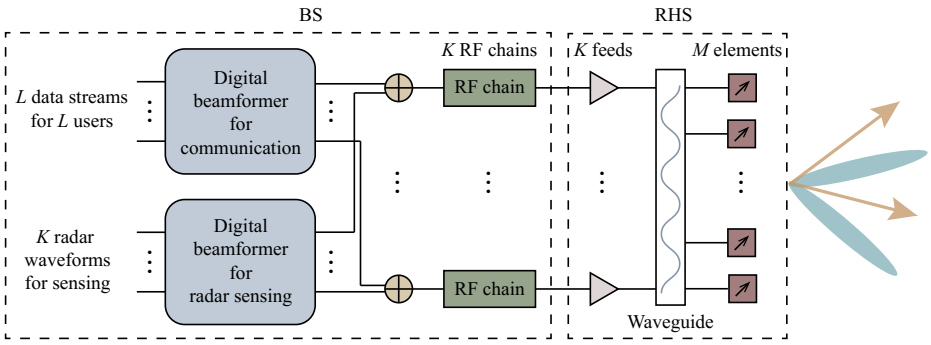

Fig. 3. Block diagram of the holographic beamforming scheme.

The function $P^c(\theta,\phi,\theta',\phi')$ characterizes the cross-correlation of the transmitted signals between the directions (θ,ϕ) and (θ',ϕ'). Let us assume that the angular region of interest is discreted into D angular grids which are denoted by $\{(\theta_1,\phi_1),\cdots,(\theta_D,\phi_D)\}$. The radar beams are designed to point towards these directions in order to examine whether targets exist in these directions. Thus, the root mean square cross-correlation can be written as [37]

$$RMSC=\sqrt{\frac{2}{D(D-1)}\sum_{d=1}^{D-1}\sum_{d'=d+1}^{D}|P^c(\theta_d,\phi_d,\theta_{d'},\phi_{d'})|^2}. \quad (19)$$

As pointed out in [13], besides the beampattern gain $P(\theta,\phi)$, the cross-correlation in (18) is a critical indicator for beampattern design as well, especially for adaptive MIMO radar techniques. Since the multi-target performance is inversely proportional to the $RMSC$, (19) needs to be minimized when designing the ISAC beampatterns.

IV. Holographic Integrated Sensing and Communication Problem Formulation

In this section, we first formulate the holographic ISAC problem in Subsection IV-A. Then, to efficiently solve the formulated problem in which the digital and analog beamforming are coupled with each other, we decouple the problem formulation into two subproblems, i.e., digital and analog beamforming, in Subsection IV-B and solve the resulting formulations.

A. Problem Formulation

The aim of the holographic ISAC problem is to optimize the radar sensing performance subject to specified SINR and power constraints. As noted in [37], the radar performance is related to the beampattern gains towards the directions of the targets and the cross-correlation among these directions. Specifically, by increasing the beampattern gains in correspondence of the direction of the targets, the SINR of the signals reflected by the targets (i.e., the echo signals) can be enhanced, leading to higher sensing performance. In addition, by decreasing the cross-correlation, it becomes easier to separate the echo signals towards different directions, which enhances the sensing accuracy as well. To characterize the radar performance, therefore, we define the radar utility function as

$$\delta=P_d-\rho RMSC, \quad (20)$$

where $P_d=\frac{1}{D}\sum_{d=1}^{D}P(\theta_d,\phi_d)$ is the average beampattern gain towards the target directions, and ρ is a weighting factor. Consequently, the optimization problem can be formulated as

$$\text{P1:}\max_{\boldsymbol{\psi},\boldsymbol{B}}\ \delta \quad (21a)$$

$$s.t.\ \gamma_d^l P(\theta_1,\phi_1)\le P(\theta_d,\phi_d)\le\gamma_d^u P(\theta_1,\phi_1), d=2,\cdots,D, \quad (21b)$$

$$\gamma_l\ge\Gamma_l, l=1,\cdots,L, \quad (21c)$$

$$\text{tr}\left(\boldsymbol{\Psi}\boldsymbol{Q}\boldsymbol{B}\boldsymbol{B}^{\text{H}}\boldsymbol{Q}^{\text{H}}\boldsymbol{\Psi}^{\text{H}}\right)=P_M, \quad (21d)$$

$$\psi_m\in\{0,\frac{1}{C^s-1},\cdots,1\}, m=1,\cdots,M, \quad (21e)$$

where γ_d^l and γ_d^u are two positive parameters controlling the beampattern gains at different directions, Γ_l is the minimum required SINR of the l-th user, and P_M is the maximum transmit power. Constraint (21b) ensures that the beampattern gains towards the directions $(\theta_{d'},\phi_{d'})$ are within the range $[\gamma_{d'}^l P(\theta_1,\phi_1),\gamma_{d'}^u P(\theta_1,\phi_1)]$, which allows us to control the beampattern gains towards different targets[6]. Constraint (21c) sets the SINR requirements for the communiation users, (21d) is the sum-power constraint for holographic beamforming[7], and (21e) accounts for the discrete values for the analog beamforming vector.

B. Problem Decomposition

Since the digital beamformer $\boldsymbol{B}$ and the analog beamformer $\boldsymbol{\psi}$ are coupled in the objective function (21a), and in the

[6]In the objective function (21a), the gain $P_d=\sum_d P(\theta_d,\phi_d)/D$ is maximized. If the relative values of the beampattern gains are not controlled, the beampattern gains at some directions may be much smaller than P_d, leading to a low detection accuracy in these directions. Thus, we use constraint (21b) to control the relative values of the beampattern gains in order to assure that $P(\theta_d,\phi_d)$ is close to P_d. In constraint (21b), we use $P(\theta_1,\phi_1)$ instead of directly setting the values of the upper and lower bounds of the beampattern gain $P(\theta_d,\phi_d)$. This is because the value of $P(\theta_d,\phi_d)$ is unknown, and the average beampattern gain P_d needs to be maximized in the objective function (21a), which makes the selection of suitable values of the bounds difficult.

[7]Constraint (21d) can be satisfied in practice by controlling the power fed into the RHS. In constraint (21d), specifically, the transmit power of the RHS P_t is restricted to P_M. Besides, the relationship between the transmit power P_t and the power fed into the RHS P_f can be expressed as $P_t=P_f e_f$, where e_f denotes the radiation efficiency, which is fixed given the size of the RHS and the material of the RHS waveguide [38]. Thus, by feeding the power $P_f=P_M/e_f$ into the RHS, the transmit power of the RHS can be set equal to P_M.

constraints (21b), (21c), and (21d), problem (P1) is difficult to tackle. To solve it efficiently, we decouple problem (P1) into two subproblems, i.e., the digital beamforming and analog beamforming subproblems.

1) Digital Beamforming: Given the analog beamforming vector $\boldsymbol{\psi}$, the digital beamforming subproblem can be written as

$$\text{P2:} \max_{\boldsymbol{B}} \ \delta \tag{22a}$$

$$s.t.\ \gamma_d^l P(\theta_1,\phi_1) \le P(\theta_d,\phi_d) \le \gamma_d^u P(\theta_1,\phi_1), d=2,\cdots,D, \tag{22b}$$

$$\gamma_l \ge \Gamma_l, l=1,\cdots,L, \tag{22c}$$

$$\text{tr}\left(\boldsymbol{\Psi Q B B}^{\text{H}}\boldsymbol{Q}^{\text{H}}\boldsymbol{\Psi}^{\text{H}}\right) = P_M. \tag{22d}$$

2) Analog Beamforming: Given the digital beamformer $\boldsymbol{B}$, the analog beamforming subproblem can be expressed as

$$\text{P3:} \max_{\boldsymbol{\psi}} \ \delta \tag{23a}$$

$$s.t.\ \gamma_d^l P(\theta_1,\phi_1) \le P(\theta_d,\phi_d) \le \gamma_d^u P(\theta_1,\phi_1), d=2,\cdots,D, \tag{23b}$$

$$\gamma_l \ge \Gamma_l, l=1,\cdots,L, \tag{23c}$$

$$\text{tr}\left(\boldsymbol{\Psi Q B B}^{\text{H}}\boldsymbol{Q}^{\text{H}}\boldsymbol{\Psi}^{\text{H}}\right) = P_M, \tag{23d}$$

$$\psi_m \in \{0, \frac{1}{C^s-1}, \cdots, 1\}, m=1,\cdots,M. \tag{23e}$$

V. Holographic Beamforming Optimization Algorithm Design

In this section, we develop a holographic beamforming optimization algorithm which solves problem (P1) in an iterative manner. In each iteration, subproblems (P2) and (P3) are tackled sequentially, and the corresponding solution methods are illustrated in Subsections V-A and V-B, respectively. The overall beampattern optimization algorithm is described in Subsection V-C.

A. Optimization of Digital Beamforming

Problem (P2) can be solved by using the semidefinite relaxation (SDR) technique. Specifically, we note that the objective function (22a) and the constraints (22b) and (22d) are determined by the matrix $\boldsymbol{R}$. Besides, the SINR constraint (22c) is only related to the matrices $\boldsymbol{R}, \boldsymbol{R}_1, \cdots, \boldsymbol{R}_L$. Thus, (P2) can be reformulated, as a function of these latter matrices, in the equivalent problem:

$$\text{P4:} \max_{\boldsymbol{R},\boldsymbol{R}_1,\cdots,\boldsymbol{R}_L} \ \text{tr}\left(\boldsymbol{A}^s\boldsymbol{R}\right) - \rho\sqrt{\text{vec}^{\text{H}}(\boldsymbol{R})\boldsymbol{Z}\text{vec}(\boldsymbol{R})} \tag{24a}$$

$$s.t.\ \text{tr}((\gamma_d^l\boldsymbol{A}(\theta_1,\phi_1) - \boldsymbol{A}(\theta_d,\phi_d))\boldsymbol{R}) \le 0, d=2,\cdots,D, \tag{24b}$$

$$\text{tr}((\gamma_d^u\boldsymbol{A}(\theta_1,\phi_1) - \boldsymbol{A}(\theta_d,\phi_d))\boldsymbol{R}) \ge 0, d=2,\cdots,D, \tag{24c}$$

$$\boldsymbol{h}_l^{\text{T}}\boldsymbol{\Psi Q}\left(\left(1+\frac{1}{\Gamma_l}\right)\boldsymbol{R}_l - \boldsymbol{R}\right)\boldsymbol{Q}^{\text{H}}\boldsymbol{\Psi}^{\text{H}}\boldsymbol{h}_l^* \ge \sigma^2, l=1,\cdots,L, \tag{24d}$$

$$\text{tr}\left(\boldsymbol{\Psi Q R Q}^{\text{H}}\boldsymbol{\Psi}^{\text{H}}\right) = P_M, \tag{24e}$$

$$\boldsymbol{R}_l \succeq 0, l=1,\cdots,L, \tag{24f}$$

$$\text{rank}(\boldsymbol{R}_l) = 1, l=1,\cdots,L, \tag{24g}$$

$$\boldsymbol{R} \succeq 0, \tag{24h}$$

$$\boldsymbol{R} - \sum_{l=1}^{L}\boldsymbol{R}_l \succeq 0, \tag{24i}$$

where (24b) and (24c) correspond to constraint (21b), and (24d) is the linear formulation of the SINR constraint (21c). Constraint (24f) ensures that the matrix $\boldsymbol{R}_l$ is positive semidefinite, and constraints (24f) and (24g) ensure that the matrix $\boldsymbol{R}_l$ can be decomposed as $\boldsymbol{R}_l = \boldsymbol{b}_l\boldsymbol{b}_l^{\text{H}}$. Constraint (24i) guarantees that $\boldsymbol{R} - \sum_{l=1}^{L}\boldsymbol{R}_l$ can be decomposed as $\boldsymbol{B}_s\boldsymbol{B}_s^{\text{H}}$. Also, we have used the following definitions:

$$\boldsymbol{A}(\theta_d,\phi_d) = \boldsymbol{Q}^{\text{H}}\boldsymbol{\Psi}^{\text{H}}\boldsymbol{a}^*(\theta_d,\phi_d)\boldsymbol{a}^{\text{T}}(\theta_d,\phi_d)\boldsymbol{\Psi Q}, \tag{25}$$

$$\boldsymbol{A}^s = \sum_{d=1}^{D}\boldsymbol{A}(\theta_d,\phi_d), \tag{26}$$

$$\boldsymbol{Z} = \frac{2}{D(D-1)}\sum_{d=1}^{D-1}\sum_{d'=d+1}^{D}\text{vec}^*(\boldsymbol{Z}_{d,d'}^{\text{T}})\text{vec}^{\text{T}}(\boldsymbol{Z}_{d,d'}^{\text{T}}), \tag{27}$$

$$\boldsymbol{Z}_{d,d'} = \boldsymbol{Q}^{\text{H}}\boldsymbol{\Psi}^{\text{H}}\boldsymbol{a}^*(\theta_{d'},\phi_{d'})\boldsymbol{a}^{\text{T}}(\theta_d,\phi_d)\boldsymbol{\Psi Q}. \tag{28}$$

Problem (P4) is non-convex due to the rank constraint (24g). According to the SDR technique, we first drop the rank constraint (24g) to obtain a relaxed version of problem (P4), which is denoted by (P4'). Since problem (P4') is convex, it can be solved effectively by using interior point methods [39]. Let us denote by $\bar{\boldsymbol{R}}, \bar{\boldsymbol{R}}_1, \cdots, \bar{\boldsymbol{R}}_L$ the optimal solution of problem (P4'). Similar to the proof in [13], a rank-one solution $\boldsymbol{R}_1, \cdots, \boldsymbol{R}_L$ of problem (P4) can be obtained as follows.

Proposition 1: Let $\boldsymbol{R}, \bar{\boldsymbol{R}}_1, \cdots, \bar{\boldsymbol{R}}_L$ denote the optimal solution of problem (P4'). A solution of problem (P4) is given by

$$\boldsymbol{R} = \bar{\boldsymbol{R}}, \tag{29}$$

$$\boldsymbol{R}_l = \frac{\bar{\boldsymbol{R}}_l\boldsymbol{Q}^{\text{H}}\boldsymbol{\Psi}^{\text{H}}\boldsymbol{h}_l^*\boldsymbol{h}_l^{\text{T}}\boldsymbol{\Psi Q}\bar{\boldsymbol{R}}_l^{\text{H}}}{\boldsymbol{h}_l^{\text{T}}\boldsymbol{\Psi Q}\bar{\boldsymbol{R}}_l\boldsymbol{Q}^{\text{H}}\boldsymbol{\Psi}^{\text{H}}\boldsymbol{h}_l^*}, l=1,\cdots,L. \tag{30}$$

Proof: See Appendix A. ■

B. Optimization of Analog Beamforming

In this subsection, we first introduce an equivalent formulation for problem (P3), and then solve the equivalent problem by using the SDR and alternating optimization (AO) methods. The equivalent reformulation of problem (P3) is given in the following proposition.

Proposition 2: Problem (P3) is equivalent to the following

$$\text{P5:} \max_{\boldsymbol{\Xi}} \text{tr}(\boldsymbol{U}_1\boldsymbol{\Xi}) - \rho\sqrt{\text{vec}^{\text{T}}(\boldsymbol{\Xi})\boldsymbol{U}_2\text{vec}(\boldsymbol{\Xi})} \tag{31a}$$

$$s.t.\ \text{tr}((\gamma_d^l\boldsymbol{U}'(\theta_1,\phi_1) - \boldsymbol{U}'(\theta_d,\phi_d))\boldsymbol{\Xi}) \le 0, d=2,\cdots,D, \tag{31b}$$

$$\text{tr}((\gamma_d^u\boldsymbol{U}'(\theta_1,\phi_1) - \boldsymbol{U}'(\theta_d,\phi_d))\boldsymbol{\Xi}) \ge 0, d=2,\cdots,D, \tag{31c}$$

$$\text{tr}\left(\left(\left(\frac{1}{\Gamma_l}+1\right)\boldsymbol{V}_l - \boldsymbol{V}_l^R\right)\boldsymbol{\Xi}\right) \ge \sigma^2, l=1,\cdots,L, \tag{31d}$$

$$\text{tr}\left(\left(\boldsymbol{QRQ}^{\text{H}} \circ \boldsymbol{I}\right)\boldsymbol{\Xi}\right) = P_M, \tag{31e}$$

$$\boldsymbol{\Xi} = \boldsymbol{\psi}^{\text{T}}\boldsymbol{\psi}, \tag{31f}$$

$$\psi_m \in \{0, \frac{1}{C^s-1}, \cdots, 1\}, m=1,\cdots,M, \tag{31g}$$

Algorithm 1: Alternating Optimization Method

Input: Quantized vector $\hat{\boldsymbol{\xi}}$;
Output: Optimized vector $\tilde{\boldsymbol{\xi}}$;
Set $t=1$, radar utility $\delta_0=-\infty$, and $\tilde{\boldsymbol{\xi}}=\hat{\boldsymbol{\xi}}$;
Compute the radar utility δ_1 using $\hat{\boldsymbol{\xi}}$;
while *the difference of the radar utilities* $\delta_t-\delta_{t-1}>\epsilon$ **do**
  Update $t=t+1$, and set $\delta_t=\delta_{t-1}$;
  for $m\in\{1,\cdots,M\}$, $\kappa\in\{0,\frac{1}{C^s-1},\cdots,1\}$ **do**
    Set $\hat{\boldsymbol{\xi}}=\tilde{\boldsymbol{\xi}}$, and replace $\hat{\xi}_m$ in $\hat{\boldsymbol{\xi}}$ with κ;
    Compute the radar utility δ' given $\hat{\boldsymbol{\xi}}$;
    if $\delta'>\delta_t$ *and* $\hat{\boldsymbol{\xi}}$ *satisfies all the constraints in (P3)* **then**
      Set $\delta_t=\delta'$ and $\tilde{\boldsymbol{\xi}}=\hat{\boldsymbol{\xi}}$;
    end
  end
end

Algorithm 2: Holographic Beamforming Optimization Algorithm

Input: SINR threshold $\{\Gamma_l\}$, and maximum transmit power P_M;
Output: Digital beamforming matrix $\boldsymbol{B}^*$ and analog beamforming vector $\boldsymbol{\psi}^*$;
Initialize N_f analog beamforming vectors $\{\boldsymbol{\psi}\}$ randomly, and obtain the digital beamforming matrices $\{\boldsymbol{B}\}$ by solving problem (P4);
The pair of digital and analog beamformers $(\boldsymbol{B}^0,\boldsymbol{\psi}^0)$ with the highest value of the radar utility are selected;
Set $t=0$;
while *the value difference of the radar utility* $\delta_t-\delta_{t-1}\geq\epsilon$ **do**
  Update $t=t+1$;
  Calculate $\boldsymbol{\psi}^t$ by solving problem (P5) given $\boldsymbol{B}^{t-1}$ and $\boldsymbol{\psi}^{t-1}$ as initial values;
  Calculate $\boldsymbol{B}^t$ by solving problem (P4) given $\boldsymbol{\psi}^t$;
  Compute radar utility δ_t given $\boldsymbol{\psi}^t$ and $\boldsymbol{B}^t$;
end
Set $\boldsymbol{B}^*=\boldsymbol{B}^t$ and $\boldsymbol{\psi}^*=\boldsymbol{\psi}^t$;

where

$$\boldsymbol{U}_1=\sum_{d=1}^{D}\boldsymbol{U}'(\theta_d,\phi_d), \tag{32}$$

$$\boldsymbol{U}'(\theta_d,\phi_d)=\boldsymbol{Q}\boldsymbol{R}\boldsymbol{Q}^{\mathrm{H}}\circ(\boldsymbol{a}^*(\theta,\phi)\boldsymbol{a}^{\mathrm{T}}(\theta,\phi))^{\mathrm{T}}, \tag{33}$$

$$\boldsymbol{U}_2=\frac{2}{D(D-1)}\sum_{d=1}^{D-1}\sum_{d'=d+1}^{D}\mathrm{vec}^*(\boldsymbol{U}_{d,d'}^{\mathrm{T}})\mathrm{vec}^{\mathrm{T}}(\boldsymbol{U}_{d,d'}^{\mathrm{T}}), \tag{34}$$

$$\boldsymbol{U}_{d,d'}=\boldsymbol{Q}\boldsymbol{R}\boldsymbol{Q}^{\mathrm{H}}\circ(\boldsymbol{a}^*(\theta_{d'},\phi_{d'})\boldsymbol{a}^{\mathrm{T}}(\theta_d,\phi_d))^{\mathrm{T}}, \tag{35}$$

$$\boldsymbol{V}_l=\boldsymbol{Q}\boldsymbol{R}_l\boldsymbol{Q}^{\mathrm{H}}\circ(\boldsymbol{H}_l^{\mathrm{H}}\boldsymbol{H}_l)^{\mathrm{T}}, \tag{36}$$

$$\boldsymbol{V}_l^R=\boldsymbol{Q}\boldsymbol{R}\boldsymbol{Q}^{\mathrm{H}}\circ(\boldsymbol{H}_l^{\mathrm{H}}\boldsymbol{H}_l)^{\mathrm{T}}. \tag{37}$$

Proof: See Appendix B. ■

To solve problem problem (P5) efficiently, we first relax the discrete constraint (31g) to a continuous constraint, as follows:

$$\psi_m\in[0,1],m=1,\cdots,M. \tag{38}$$

The relaxed problem is a quadratic program and can be solved using the SDR method [40]. In the SDR method, we utilize the SeDuMi solver in the CVX toolbox [12]. Let $\bar{\boldsymbol{\xi}}$ denote the solution of the relaxed problem. The elements of $\bar{\boldsymbol{\xi}}$ are quantized to the nearest values in $\{0,\frac{1}{C^s-1},\cdots,1\}$ so as to satisfy the discrete constraint (31g). Let $\hat{\boldsymbol{\xi}}$ denote the obtained quantized vector. The vector $\hat{\boldsymbol{\xi}}$ is further optimized with the aid of the AO method, as shown in Algorithm 1. Specifically, each element of $\hat{\boldsymbol{\xi}}$ is optimized sequentially in each iteration of the AO method. For each element of the vector, we first enumerate the objective function in (22a) for all possible values in the set $\{0,\frac{1}{C^s-1},\cdots,1\}$ and then select the largest value of the objective function that satisfies all the constraints in problem (P3). The algorithm terminates when the difference of the values of objective function (23a) in two consecutive iterations is smaller than a small threshold ϵ.

C. Overall Algorithm

In this subsection, the complete holographic beamforming optimization algorithm is proposed based on the algorithms introduced in the last two subsections. The proposed algorithm consists of the following steps. First, we randomly select N_f analog beamforming vectors denoted by set $\{\boldsymbol{\psi}\}$. Next, for each vector $\boldsymbol{\psi}$ in $\{\boldsymbol{\psi}\}$, we solve problem (P4) and obtain the corresponding digital beamformer $\boldsymbol{B}$. Let $(\boldsymbol{B}^0,\boldsymbol{\psi}^0)$ denote the pair of beamformers with the highest value of the radar utility. Subsequently, the beamformers $(\boldsymbol{B}^0,\boldsymbol{\psi}^0)$ are optimized iteratively. At the t-th iteration, specifically, we solve problem (P5) and obtain $\boldsymbol{\psi}^t$ given the digital beamformer $\boldsymbol{B}^{t-1}$. In the meantime, $\boldsymbol{\psi}^{t-1}$ is also optimized using the AO method. The values of the radar utility are calculated using $\boldsymbol{\psi}'$ and the optimized $\boldsymbol{\psi}^{t-1}$, and the utility with a higher value is set to $\boldsymbol{\psi}^t$. Then, subproblem (P4) is solved again to obtain $\boldsymbol{B}^t$ given the optimized analog beamformer $\boldsymbol{\psi}^t$. Let δ_t denote the value of the radar utility that is computed by using the digital beamformer $\boldsymbol{B}^t$ and analog beamformer $\boldsymbol{\psi}^t$. The algorithm ends when the difference between the radar utility functions of two consecutive iterations is less than ϵ, i.e., $\delta_t-\delta_{t-1}<\epsilon$. In this way, we can assure that the value of the radar utility is increased by at least ϵ in each iteration. The complete holographic beamforming optimization algorithm is summarized in Algorithm 2.

VI. Performance Analysis

In this section, we first investigate the beampattern gain offered by the holographic beamforming in Subsection VI-A. Then, the convergence and complexity of the proposed holographic beamforming optimization algorithm are discussed in Subsection VI-B. Finally, the cost effectiveness of the proposed scheme is analyzed in Subsection VI-C.

A. Beampattern Gain Analysis

In this subsection, we analyze the maximum beampattern gain of the RHS, which represents the ability of an antenna to concentrate the transmit power in a given direction [41]. As far as the holographic beamforming is concerned, we cannot derive a closed-form expression for the optimal digital and analog beamformer vectors with maximum beampattern gain towards the direction of the target under the sum-power constraint since the holographic beamforming optimization problem is an integer program. As an alternative, a lower bound for the maximum beampattern gain under of the sum-power constraint is provided by the following proposition.

Proposition 3: Consider an RHS with a sufficiently large number of metamaterial elements, a lower bound for the maximum beampattern gain at a given direction under the sum-power constraint can be approximated by:

$$P_L \approx \frac{P_M M}{6}. \tag{39}$$

Proof: See Appendix C. ∎

Based on Proposition 3, we can compare the beamforming capabilities between an RHS and a traditional HAD-based MIMO array with the same size. The maximum beampattern gain of a HAD-based MIMO array towards a given direction under the sum-power constraint is given by [42]:

$$P_A = M_A P_M, \tag{40}$$

where M_A denotes the number of antennas in the MIMO array. Thus, when M is sufficiently large, the ratio between the maximum beampattern gain, P_R, of an RHS and the maximum beampattern gain of a MIMO array of the same size can be expressed as:

$$\iota = \frac{P_R}{P_A} \geq \frac{P_L}{P_A} \approx \frac{M}{6M_A}. \tag{41}$$

From (41) we evince that $\iota > 1$ if $M/M_A > 6$. This implies that an RHS outperforms a traditional MIMO array of the same size in terms of beamforming gain when M is sufficiently large. Since the element spacing in an MIMO array is typically half of the wavelength, and the element spacing in an RHS is on the order of $\lambda/10$ [23], the number of elements in an RHS can be 25 times larger than that in a MIMO array, which indicates that the beamforming gain can be significantly increased by using an RHS.

B. Convergence and Complexity

1) Convergence: In the following proposition, we provide a lower bound and an upper bound for the radar utility function.

Proposition 4: The radar utility function δ is lower and upper bounded as

$$-\rho M P_M \leq \delta \leq M P_M. \tag{42}$$

Proof: See Appendix D. ∎

Since the radar utility is within the range $[-\rho M P_M, M P_M]$, and the radar utility is increased by at least ϵ in each iteration of the holographic beamforming optimization algorithm, the maximum number of iterations is $\lceil (1+\rho) M P_M/\epsilon \rceil$, which indicates that the algorithm is guaranteed to converge[8].

2) Complexity: At the beginning of the holographic beamforming optimization algorithm, (P4) is solved for N_f times by using the SDR method whose complexity is $O(K^{4.5}\log(1/\zeta))$ [40], where ζ is the solution accuracy of the interior-point algorithm. Thus, the complexity of this step is $O(N_f K^{4.5}\log(1/\zeta))$.

Then, the beamformers $\boldsymbol{B}$ and $\boldsymbol{\psi}$ are optimized in an iterative manner. In each iteration, problem (P5) is first utilized to optimize $\boldsymbol{\psi}$ with the aid of the SDR and AO methods. The complexity of the SDR method for solving problem (P5) is $O(M^{4.5}\log(1/\zeta))$. As for the AO method, the maximum number of iterations is $\lceil (1+\rho) M P_M/\epsilon \rceil$. Since the complexity of each iteration is $O(M^2)$, the complexity of the AO method is $O(M^3)$. Finally, problem (P4) is solved, whose complexity is $O(K^{4.5}\log(1/\zeta))$. Thus, the complexity of each iteration of the holographic beamforming optimization algorithm is $O((K^{4.5}+M^{4.5})\log(1/\zeta))$.

Based on (42), the maximum number of iterations of the holographic beamforming optimization algorithm is $(1+\rho) M P_M/\epsilon$. Thus, the overall complexity is $O(((N_f + M)K^{4.5} + M^{5.5})\log(1/\zeta))$.

C. Cost-Effectiveness Analysis

In this subsection, we analyze the cost-effectiveness of the proposed ISAC scheme. The cost-effectiveness is defined as the cost saving of using an RHS instead of using a traditional HAD-based MIMO array. For fairness, we assume that both systems have the same radar utility function δ. We utilize the following efficiency metric [43]:

$$\eta(\delta) = 1 - \alpha_r(\delta)/\alpha_a(\delta), \tag{43}$$

where $\alpha_r(\delta)$ is the cost of the RHS to obtain the radar utility δ, and $\alpha_a(\delta)$ is the cost of the HAD-based MIMO array to obtain the same utility δ. From (43) we obtain that $\eta(\delta) > 0$ when the cost of the RHS is lower than the cost of the HAD-based MIMO array. Also, a larger value of $\eta(\delta)$ indicates a greater cost saving when using the RHS.

Let us assume that the hardware cost of each metamaterial element is ν. Then, the cost of an RHS is $\alpha_r(\delta) = \nu M + \chi K$, where χ is the cost of one RF chain. Similarly, the hardware cost of a HAD-based MIMO array is $\alpha_a(\delta) = \beta\nu M_A + \chi K$, where β denotes the ratio of the cost of one antenna in the HAD-based MIMO array to the cost of a metamaterial element.

For simplicity, we consider the case study of a beampattern with one main lobe and ignore the SINR constraints. For a MIMO array, thus, we have $\delta = P_A = M_A P_M$, and its cost is given by:

$$\alpha_a(\delta) = \frac{\beta\nu\delta}{P_M} + \chi K. \tag{44}$$

[8]The solution of the algorithm is also guaranteed to converge. This is because, in each iteration, we obtain a unique solution and the corresponding value of the objective function. Let $(\boldsymbol{B}^t, \boldsymbol{\psi}^t)$ and δ_t denote the solution and the value of the radar utility function in the t-th iteration. Since we have proved the convergence of the radar utility function, without loss of generality, we assume that the radar utility converges to $\delta_{t'}$. This indicates that the algorithm terminates in the t'-th iteration, and the solution converges to $(\boldsymbol{B}^{t'}, \boldsymbol{\psi}^{t'})$.

TABLE I
MAIN SIMULATION PARAMETERS

Parameters	**Values**
Center of the RHS r_r	$(0,0,0)$
Number of metamaterial elements M	$36 \sim 144$
Number of quantization bits N_b	3
Number of phase shifts C^s	8
Inter-distance between metamaterial elements d_s	$\lambda/6$
Inter-distance between MIMO antennas d_m	$\lambda/2$
Refractive index of the waveguide substrate n_r	$\sqrt{3}$
Number of feeds K	$4 \sim 6$
Maximum transmit power of the RHS P_M	1W
Number of communication users L	$2 \sim 4$
SINR threshold Γ_l	$4 \sim 12$dB
Variance of the noise σ^2	0.01

As for holographic beamforming, based on Proposition 3, when M is sufficiently large, a lower bound for the RHS cost is given by:

$$\alpha_r(\delta) \leq \frac{6\nu\delta}{P_M} + \chi K. \tag{45}$$

According to (44) and (45), the cost-effectiveness can be approximated as follows:

$$\eta(\delta) \geq 1 - \frac{6\nu\delta + P_M\chi K}{\beta\nu\delta + P_M\chi K}. \tag{46}$$

If $\beta > 6$, we evince from (46) that $\eta(\delta)$ is guaranteed to be greater than 0 for any δ, which provides the condition under which an RHS is more cost-effective than a HAD-based MIMO array. It is worth noting that the antennas in a HAD-based MIMO array usually require many expensive components, such as phase shifters and power amplifiers for beam steering. In practice, therefore, it is expected that the cost ratio is much greater than 6 [24], which shows the potential cost-effectiveness of using holographic beamforming.

VII. SIMULATION RESULTS

In this section, numerical results illustrating the performance of the proposed ISAC scheme are presented. We assume that the RHS is located in the plane $x = 0$, and that the center of the RHS is at the origin. The inter-distance between the metamaterial elements is $\lambda/6$ [23], where λ is the wavelength in free space. The RHS comprises $4 \sim 6$ feeds, and each of them is connected to an RF chain. The maximum transmit power of the RHS is 1W. The refractive index of the substrate in the parallel-plate waveguide is $\sqrt{3}$, and thus the absolute value of the propagation vector is $|\boldsymbol{k}_m^k| = \sqrt{3}|\boldsymbol{k}_f(\theta,\phi)| = 2\pi\sqrt{3}f/v_c$, where f is the carrier frequency of the transmitted signal, and v_c is the speed of light. The number of users is $L = 2, 3, 4$, and the SINR threshold Γ_l varies from 4dB to 12dB. The communication channels between the RHS and the users are Rayleigh distributed, i.e., the channel $h_{l,m}$ follows a standard complex Gaussian distribution with mean 0 and variance 1. The variance of the noise is $\sigma^2 = 0.01$. The main parameters of the simulation setup are listed in Table I.

A. Holographic Beamforming Performance

Fig. 4 illustrates the normalized beampattern of the RHS with three main lobes. The normalized beampattern is defined as

$$P^n(\theta,\phi) = \frac{P(\theta,\phi)}{P_G}, \tag{47}$$

where P_G is the maximum beampattern gain. The beampattern is obtained by setting 3 directions of interest $(\pi/4, 0)$, $(\pi/4, \pi)$, and $(\pi/4, 3\pi/2)$. The RHS comprises $M = 12 \times 12$ elements and 5 feeds. The parameters γ_d^l and γ_d^u are set equal to 0.9 and 1.1, respectively, to control the beampattern gains towards different directions. The number of users is $L = 2$, and the SINR threshold is $\Gamma = 4$dB. We observe that the main lobes point towards the target directions, and the levels of the side lobes are relatively low compared with those of the main lobes. This indicates that the RHS is able to simultaneously steer the beams towards the directions of interest for sensing and to serve communication users.

Fig. 5 shows the SINR of the users γ_l in different simulation rounds when the number of users is $I = 2$. The SINR threshold for all the users is 8dB. We see that the SINRs of all the users are equal to or higher than the 8dB threshold in different simulation rounds, which means that the SINR threshold is successfully achieved for all the users by using holographic beamforming.

B. Comparison with the HAD-based MIMO Scheme

Fig. 6 shows the maximum beampattern gain P_G versus the edge length of the antenna aperture l_a. For comparison, we illustrate the maximum beampattern gains obtained by the lower bound provided in Proposition 3 and that obtained by a HAD-based MIMO array using (40). We observe that the maximum beampattern gain P_G increases with the edge length of the antenna aperture for different schemes. Besides, we can observe that the maximum beampattern gain obtained by the proposed scheme is higher than that obtained by the lower bound, which is in accordance with the analysis in Subsection VI-A. In addition, compared with the MIMO based scheme, the maximum beampattern gains obtained by the RHS based schemes with the same antenna aperture are increased by at least 50%, which shows the superiority of the holographic beamforming in enhancing the maximum beamforming gain.

Fig. 7 illustrates the cost-effectiveness η of the proposed scheme with respect to a HAD-based MIMO scheme as a function of the radar utility δ for different values of cost ratio β when $\rho = 0.8$. As discussed in Section VI-C, the cost-effectiveness quantifies the cost saving of using the proposed scheme in lieu of a HAD-based MIMO scheme with the same radar utility. A positive value of cost-effectiveness implies that the cost of the RHS is smaller than that of the MIMO array, and a larger value of the cost-effectiveness implies that a larger cost saving in favor of the RHS. We observe that, for different values of the cost ratio β, the cost-effectiveness is alway greater than 0. Besides, we note that the cost-effectiveness η increases with the radar utility δ, which indicates that larger cost savings can be obtained with the proposed scheme when more stringent performance requirements are imposed.

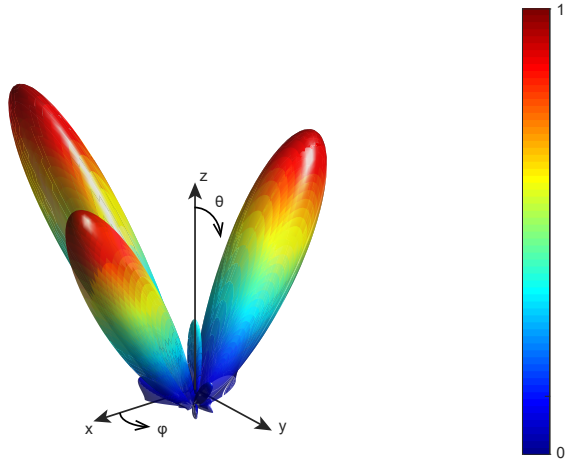

Fig. 4. Normalized beampattern of the RHS with three main lobes.

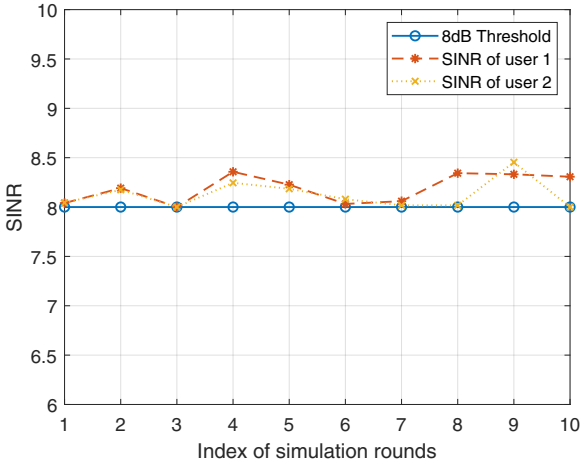

Fig. 5. SINR of users γ_l in different simulation rounds.

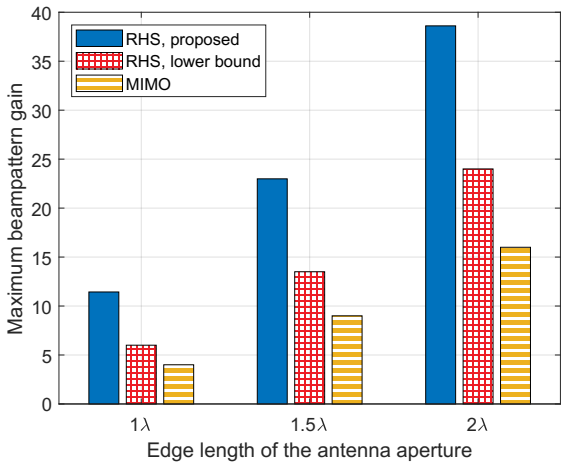

Fig. 6. Maximum beampattern gain P_G versus the edge length of the antenna aperture l_a.

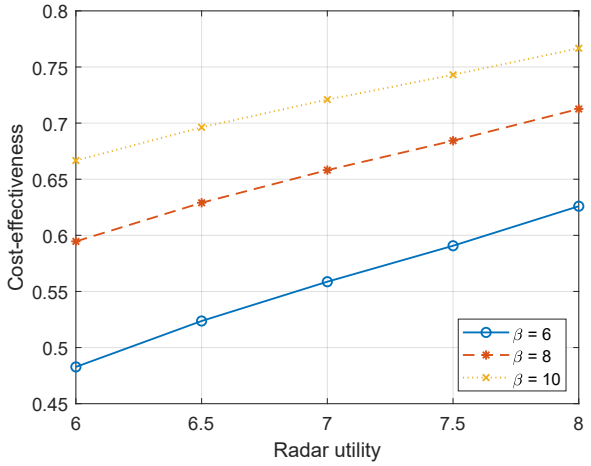

Fig. 7. Cost-effectiveness η of the proposed scheme over the HAD-based scheme versus the radar utility δ for different values of cost ratio β.

Fig. 8 shows the average beampattern gain $\bar{P}$ towards the desired directions and the root mean square cross-correlation $RMSC$ as a function of the weighting factor ρ for the proposed scheme and the HAD-based MIMO scheme. When $\rho = 0$, which indicates that the cross-correlation $RMSC$ is not taken into account in the objective function, we observe that the value of cross-correlation $RMSC$ is close to the average beampattern gain P_d, which implies that the transmit signals in the the target directions are highly correlated. When the weighting factor ρ increases, we observe that both the average beampattern gain $\bar{P}$ and the root mean square cross-correlation $RMSC$ decrease, and that $RMSC$ becomes close to 0 for both the proposed and MIMO based scheme when $\rho \geq 0.8$. This indicates that by setting a large value of ρ, the signals emitted in different target directions are uncorrelated and allow one to accurately discriminate targets in different directions. In addition, when $\rho \geq 0.8$, the average beampattern obtained by the proposed scheme is higher than that obtained by the MIMO based scheme, which shows that compared with the MIMO based scheme, the proposed scheme can emit uncoorelated signals with higher beampattern gain.

To compare the detection probabilities of the proposed and HAD-based MIMO schemes, the generalized likelihood ratio test (GLRT) is performed, which is widely used for target detection [44], [45]. We assume that there are two directions of interest $(\pi/4, 0)$ and $(\pi/4, \pi)$. Thus, the possible detection results can be represented by four hypotheses, which are expressed as

$$\begin{cases} \mathcal{H}_0 : \text{no target exists,} \\ \mathcal{H}_1 : \text{a target exists in direction } (\pi/4, 0), \\ \mathcal{H}_2 : \text{a target exists in direction } (\pi/4, \pi), \\ \mathcal{H}_3 : \text{two target exists in } (\pi/4, 0) \text{ and } (\pi/4, \pi), \text{ respectively.} \end{cases}$$

In the simulation setting, we set a target with reflection coefficient 0.02 in direction $(\pi/4, 0)$, which means that the correct hypothesis is $\mathcal{H}_1$. The false alarm probability of the GLRT test is set as 0.0001.

Fig. 9 shows the detection probability $p_d = p(\mathcal{H}_1|\mathcal{H}_1)$ of the proposed and the HAD-based MIMO schemes versus the weighting factor ρ when the edge length of the antenna aperture $l_a = 1.5\lambda$. We observe that the detection probabilities of the two schemes increase with the weighting factor when $\rho < 0.8$ and remain constant when $\rho \geq 0.8$. This is because

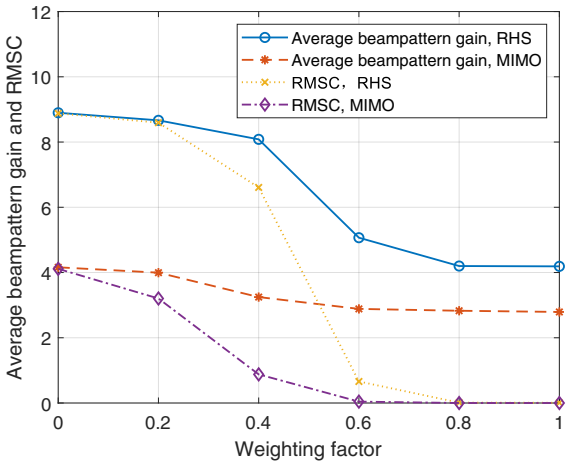

Fig. 8. Average beampattern gain $\bar{P}$ evaluated at the target directions and the root mean square cross-correlation $RMSC$ versus the weighting factor ρ.

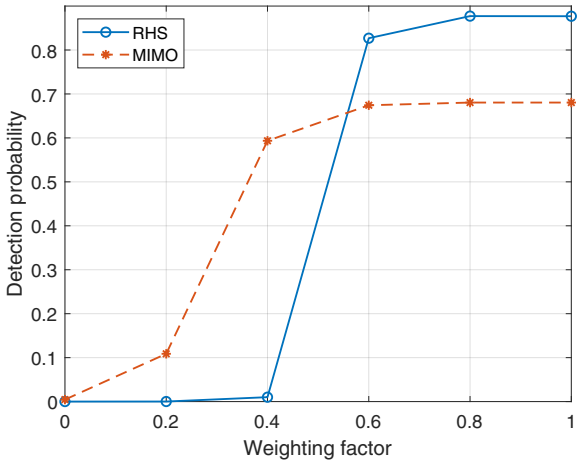

Fig. 9. Detection probability p_d versus the weighting factor ρ.

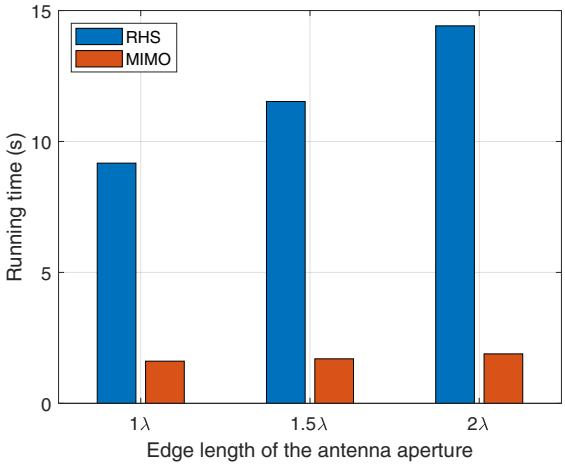

Fig. 10. Running time t_r versus the edge length of the antenna aperture l_a.

the cross-correlation of the transmitted signals in the two directions, i.e., the $RMSC$, is inversely proportional to ρ when $\rho < 0.8$, leading to a better accuracy of the identification of the targets towards different directions when ρ increases. In addition, the detection probability of the proposed scheme is higher than that of the MIMO based scheme when $\rho = 1$, which validates the effectiveness of the proposed scheme.

Fig. 10 depicts the running time t_r of the proposed and HAD-based MIMO schemes versus the edge length of the antenna aperture l_a. The running time is obtained using a computer equipped with an Intel Core i7-7700 CPU and Matlab 2019b. We observe that the running time of the two schemes increases with the edge length of the antenna aperture, and the proposed scheme requires a longer running time than the HAD-based MIMO scheme given the same antenna aperture. This is because the radiation amplitudes of numerous elements need to be optimized in the proposed scheme, while the phase shifts of a smaller number of phase shifters are optimized in an HAD-based MIMO array with the same antenna aperture.

C. Impact of the RHS on the System Performance

Fig. 11 depicts the radar utility δ as a function of the SINR threshold Γ for a different number of feeds K in the RHS when $\rho = 0.8$. We observe that the radar utility δ decreases when the SINR threshold Γ increases, which implies that the sensing performance is reduced in order to provide higher communication rates to the users. Besides, the radar utility δ increases with the number of feeds while keeping the SINR threshold fixed. This is because a larger number of RHS feeds provides more degrees of freedom for digital beamforming, which positively contributes to the radar and communication performance.

Fig. 12 shows the radar utility δ as a function of the number of users L for a different size of the RHS when the SINR threshold is $\Gamma = 4$dB. We observe that δ decreases when the number of users L increases. However, we observe that δ increases with the size of the RHS. This demonstrates that, by increasing the RHS size, the proposed system is able to support more users and to synthesize beams with a larger radar utility, which is beneficial for ISAC systems.

Fig. 13 shows the radar utility δ versus the number of elements M for a different number of feeds K in the RHS. We observe that the radar utility increases with the number of elements M and the number of feeds K. This indicates that, to obtain a given radar utility, we can use an RHS with more elements and fewer feeds or vice versa. Besides, Fig. 14 presents the radar utility δ versus the number of elements M for a different number of quantization bits N_b. We see that the radar utility increases with the number of elements M and the number of quantization bits N_b. This is because the radiation amplitudes of each RHS element can be tuned with a finer resolution by increasing N_b, which promotes the beam-steering capabilities of the RHS.

VIII. Conclusion

In this paper, we have considered an RHS-aided ISAC system where the MIMO array employed in traditional ISAC systems is replaced by an RHS to perform holographic

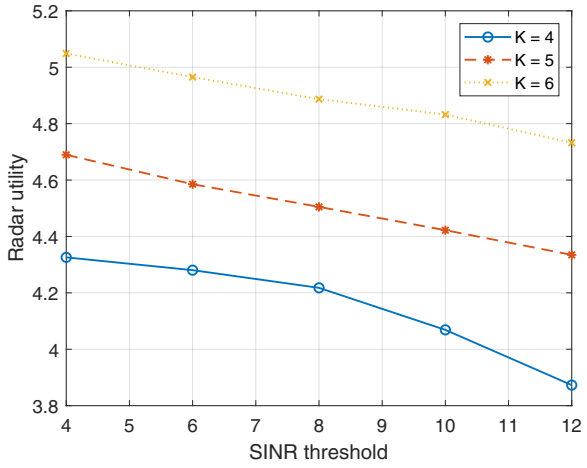

Fig. 11. Radar utility δ versus the SINR threshold Γ for a different number of feeds K in the RHS.

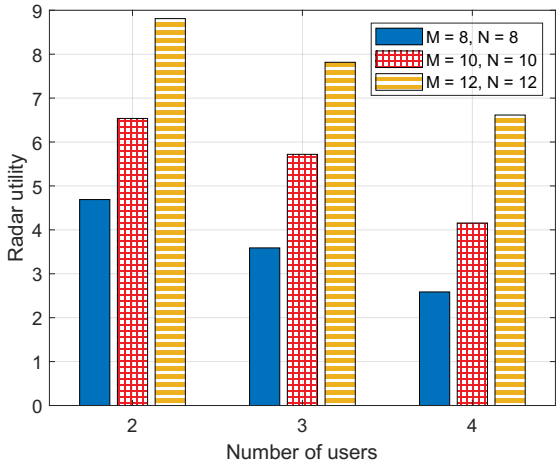

Fig. 12. Radar utility δ versus the number of users L for a different size of the RHS.

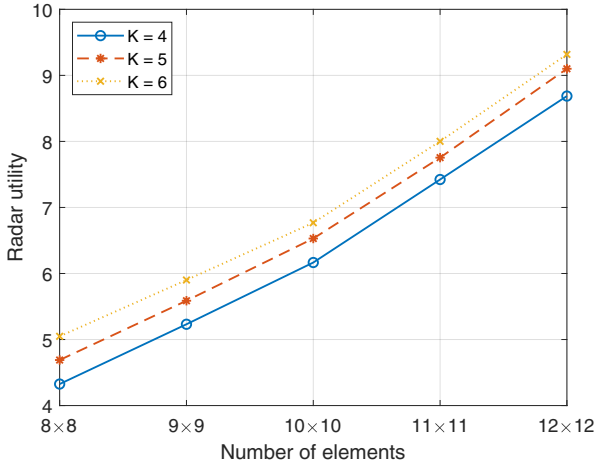

Fig. 13. Radar utility δ versus the number of elements M for a different number of feeds K in the RHS.

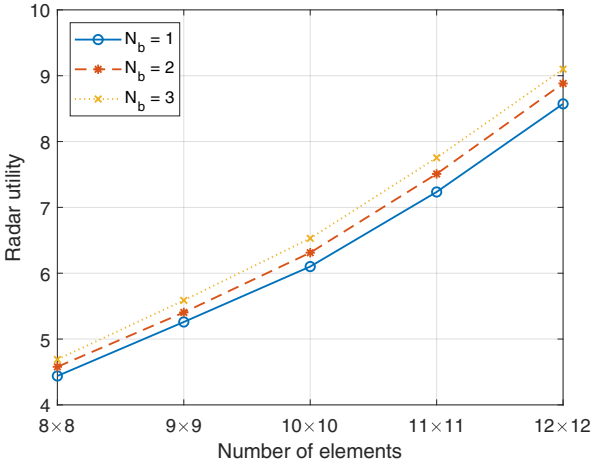

Fig. 14. Radar utility δ versus the number of elements M for a different number of quantization bits N_b.

beamforming for radar and communication functionalities. We have formulated a holographic integrated sensing and communication optimization problem for improving the radar performance subject to specified SINR requirements for the communication users. To efficiently solve the formulated problem, we have proposed a holographic beamforming algorithm that optimizes the digital beamformer at the BS and the analog beamformer at the RHS in an iterative manner. We have provided a lower bound for the maximum beampattern gain of a large-scale RHS through theoretical analysis. Specifically, we have proved that a higher maximum beampattern gain can be obtained using an RHS with a compact deployment of metamaterial elements compared with that obtained by a MIMO array. Simulation results have shown that: 1) the maximum beamforming gain of an RHS can be at least 50% larger than that of a traditional HAD-based MIMO array with the same size; 2) the cost of the proposed scheme is smaller than that of the HAD-based MIMO scheme with the same performance, and more cost can be saved by using holographic beamforming when a higher performance requirement is imposed; and 3) the radar and communication performance can be enhanced by increasing the number of feeds or the size of the RHS.

Appendix A
Proof of Proposition 1

To show that the matrices $\boldsymbol{R}, \boldsymbol{R}_1, \cdots, \boldsymbol{R}_L$ obtained by using (29) and (30) are a solution of (P4), we need to prove that the matrices $\boldsymbol{R}, \boldsymbol{R}_1, \cdots, \boldsymbol{R}_L$ satisfy all the constraints of problem (P4).

First, since $\boldsymbol{R} = \bar{\boldsymbol{R}}$ and the constraints (24b), (24c), (24e), and (24h) are only determined by $\boldsymbol{R}$, these constraints are satisfied. Besides, according to (30), we have

$$\begin{aligned}\boldsymbol{h}_l^{\mathrm{T}}\boldsymbol{\Psi}\boldsymbol{Q}\boldsymbol{R}_l\boldsymbol{Q}^{\mathrm{H}}\boldsymbol{\Psi}^{\mathrm{H}}\boldsymbol{h}_l^* &= \frac{\boldsymbol{h}_l^{\mathrm{T}}\boldsymbol{\Psi}\boldsymbol{Q}\bar{\boldsymbol{R}}_l\boldsymbol{Q}^{\mathrm{H}}\boldsymbol{\Psi}^{\mathrm{H}}\boldsymbol{h}_l^*\boldsymbol{h}_l^{\mathrm{T}}\boldsymbol{\Psi}\boldsymbol{Q}\bar{\boldsymbol{R}}_l^{\mathrm{H}}\boldsymbol{Q}^{\mathrm{H}}\boldsymbol{\Psi}^{\mathrm{H}}\boldsymbol{h}_l^*}{\boldsymbol{h}_l^{\mathrm{T}}\boldsymbol{\Psi}\boldsymbol{Q}\bar{\boldsymbol{R}}_l\boldsymbol{Q}^{\mathrm{H}}\boldsymbol{\Psi}^{\mathrm{H}}\boldsymbol{h}_l^*} \\ &= \boldsymbol{h}_l^{\mathrm{T}}\boldsymbol{\Psi}\boldsymbol{Q}\bar{\boldsymbol{R}}_l\boldsymbol{Q}^{\mathrm{H}}\boldsymbol{\Psi}^{\mathrm{H}}\boldsymbol{h}_l^*, \end{aligned} \tag{47}$$

which means that the SINR constraint (24d) is fulfilled as well.

In addition, based on (30), the rank of $\boldsymbol{R}_l$ is

$$\mathrm{rank}(\boldsymbol{R}_l) \leq \min(\mathrm{rank}(\bar{\boldsymbol{R}}), \mathrm{rank}(\boldsymbol{Q}), \mathrm{rank}(\boldsymbol{\Psi}), \mathrm{rank}(\boldsymbol{h}_l)) = 1. \tag{48}$$

Since $\boldsymbol{R}_l$ is not a zero matrix, we have $\mathrm{rank}(\boldsymbol{R}_l) \geq 1$, and thus $\mathrm{rank}(\boldsymbol{R}_l) = 1$.

As for constraint (24f), we have

$$\boldsymbol{v}^{\mathrm{H}}\boldsymbol{R}_l\boldsymbol{v}=\frac{\boldsymbol{v}^{\mathrm{H}}\bar{\boldsymbol{R}}_l\boldsymbol{Q}^{\mathrm{H}}\boldsymbol{\Psi}^{\mathrm{H}}\boldsymbol{h}_l^*\boldsymbol{h}_l^{\mathrm{T}}\boldsymbol{\Psi}\boldsymbol{Q}\bar{\boldsymbol{R}}_l^{\mathrm{H}}\boldsymbol{v}}{\boldsymbol{h}_l^{\mathrm{T}}\boldsymbol{\Psi}\boldsymbol{Q}\bar{\boldsymbol{R}}_l\boldsymbol{Q}^{\mathrm{H}}\boldsymbol{\Psi}^{\mathrm{H}}\boldsymbol{h}_l^*}=\frac{|\boldsymbol{h}_l^{\mathrm{T}}\boldsymbol{\Psi}\boldsymbol{Q}\bar{\boldsymbol{R}}_l^{\mathrm{H}}\boldsymbol{v}|^2}{\boldsymbol{h}_l^{\mathrm{T}}\boldsymbol{\Psi}\boldsymbol{Q}\bar{\boldsymbol{R}}_l\boldsymbol{Q}^{\mathrm{H}}\boldsymbol{\Psi}^{\mathrm{H}}\boldsymbol{h}_l^*} \tag{49}$$

where $\boldsymbol{v}$ is an arbitrary vector in the set $\mathbb{C}^{K\times 1}$. Since $|\boldsymbol{h}_l^{\mathrm{T}}\boldsymbol{\Psi}\boldsymbol{Q}\bar{\boldsymbol{R}}_l^{\mathrm{H}}\boldsymbol{v}|^2\geq 0$ and $\boldsymbol{h}_l^{\mathrm{T}}\boldsymbol{\Psi}\boldsymbol{Q}\bar{\boldsymbol{R}}_l\boldsymbol{Q}^{\mathrm{H}}\boldsymbol{\Psi}^{\mathrm{H}}\boldsymbol{h}_l^*>0$, we have $\boldsymbol{R}_l\succeq 0$.

Finally, the verification of constraint (24i) is similar to that in [13], which is omitted for brevity. Therefore, the proof of Proposition 1 is completed.

Appendix B
Proof of Proposition 2

The beampattern gain evaluated at the direction (θ,ϕ) can be expressed as

$$\begin{aligned}P(\theta,\phi)=&\ \boldsymbol{a}^{\mathrm{T}}(\theta,\phi)\boldsymbol{\Psi}\boldsymbol{Q}\boldsymbol{R}\boldsymbol{Q}^{\mathrm{H}}\boldsymbol{\Psi}^{\mathrm{H}}\boldsymbol{a}^*(\theta,\phi)\\ =&\ \mathrm{tr}(\boldsymbol{\Psi}\boldsymbol{Q}\boldsymbol{R}\boldsymbol{Q}^{\mathrm{H}}\boldsymbol{\Psi}\boldsymbol{a}^*(\theta,\phi)\boldsymbol{a}^{\mathrm{T}}(\theta,\phi))\\ =&\ \boldsymbol{\psi}(\boldsymbol{Q}\boldsymbol{R}\boldsymbol{Q}^{\mathrm{H}}\circ(\boldsymbol{a}^*(\theta,\phi)\boldsymbol{a}^{\mathrm{T}}(\theta,\phi))^{\mathrm{T}})\boldsymbol{\psi}^{\mathrm{T}}\\ =&\ \boldsymbol{\psi}\boldsymbol{U}'(\theta,\phi)\boldsymbol{\psi}^{\mathrm{T}},\end{aligned} \tag{50}$$

where

$$\boldsymbol{U}'(\theta,\phi)=\boldsymbol{Q}\boldsymbol{R}\boldsymbol{Q}^{\mathrm{H}}\circ(\boldsymbol{a}^*(\theta,\phi)\boldsymbol{a}^{\mathrm{T}}(\theta,\phi))^{\mathrm{T}}. \tag{51}$$

Thus, the first term of the objective function (23a) can be expressed as

$$\sum_{d=1}^{D}P(\theta_d,\phi_d)=\sum_{d=1}^{D}\boldsymbol{\psi}\boldsymbol{U}'(\theta_d,\phi_d)\boldsymbol{\psi}^{\mathrm{T}}=\boldsymbol{\psi}\boldsymbol{U}_1\boldsymbol{\psi}^{\mathrm{T}}=\mathrm{tr}(\boldsymbol{U}_1\boldsymbol{\Xi}), \tag{52}$$

where $\boldsymbol{U}_1=\sum_{d=1}^{D}\boldsymbol{U}'(\theta_d,\phi_d)$ and $\boldsymbol{\Xi}=\boldsymbol{\psi}^{\mathrm{T}}\boldsymbol{\psi}$.

Also, the second term of the objective function (23a) can be written as

$$\begin{aligned}&RMSC\\ =&\sqrt{\frac{2}{D(D-1)}\sum_{d=1}^{D-1}\sum_{d'=d+1}^{D}|\boldsymbol{a}^{\mathrm{T}}(\theta_d,\phi_d)\boldsymbol{\Psi}\boldsymbol{Q}\boldsymbol{R}\boldsymbol{Q}^{\mathrm{H}}\boldsymbol{\Psi}^{\mathrm{H}}\boldsymbol{a}^*(\theta_{d'},\phi_{d'})|^2}\\ =&\sqrt{\frac{2}{D(D-1)}\sum_{d=1}^{D-1}\sum_{d'=d+1}^{D}|\boldsymbol{\psi}(\boldsymbol{Q}\boldsymbol{R}\boldsymbol{Q}^{\mathrm{H}}\circ(\boldsymbol{a}^*(\theta_{d'},\phi_{d'})\boldsymbol{a}^{\mathrm{T}}(\theta_d,\phi_d))^{\mathrm{T}})\boldsymbol{\psi}^{\mathrm{T}}|^2}\\ =&\sqrt{\frac{2}{D(D-1)}\sum_{d=1}^{D-1}\sum_{d'=d+1}^{D}|\mathrm{tr}(\boldsymbol{U}_{d,d'}\boldsymbol{\Xi})|^2}\\ =&\sqrt{\frac{2}{D(D-1)}\sum_{d=1}^{D-1}\sum_{d'=d+1}^{D}\left|\mathrm{vec}^{\mathrm{T}}(\boldsymbol{U}_{d,d'}^{\mathrm{T}})\mathrm{vec}(\boldsymbol{\Xi})\right|^2}\\ =&\sqrt{\mathrm{vec}^{\mathrm{T}}(\boldsymbol{\Xi})\boldsymbol{U}_2\mathrm{vec}(\boldsymbol{\Xi})},\end{aligned} \tag{53}$$

where

$$\boldsymbol{U}_{d,d'}=\boldsymbol{Q}\boldsymbol{R}\boldsymbol{Q}^{\mathrm{H}}\circ(\boldsymbol{a}^*(\theta_{d'},\phi_{d'})\boldsymbol{a}^{\mathrm{T}}(\theta_d,\phi_d))^{\mathrm{T}}, \tag{54}$$

$$\boldsymbol{U}_2=\frac{2}{D(D-1)}\sum_{d=1}^{D-1}\sum_{d'=d+1}^{D}\mathrm{vec}^*(\boldsymbol{U}_{d,d'}^{\mathrm{T}})\mathrm{vec}^{\mathrm{T}}(\boldsymbol{U}_{d,d'}^{\mathrm{T}}). \tag{55}$$

As for the SINR constraint (31d), it can be written as

$$\begin{aligned}&\gamma_l\geq\Gamma_l\\ &\frac{\boldsymbol{\psi}(\boldsymbol{Q}\boldsymbol{R}_l\boldsymbol{Q}^{\mathrm{H}}\circ(\boldsymbol{H}_l^{\mathrm{H}}\boldsymbol{H}_l)^{\mathrm{T}})\boldsymbol{\psi}^{\mathrm{T}}}{\boldsymbol{\psi}(\boldsymbol{Q}\boldsymbol{R}\boldsymbol{Q}^{\mathrm{H}}\circ(\boldsymbol{H}_l^{\mathrm{H}}\boldsymbol{H}_l)^{\mathrm{T}})\boldsymbol{\psi}^{\mathrm{T}}-\boldsymbol{\psi}(\boldsymbol{Q}\boldsymbol{R}_l\boldsymbol{Q}^{\mathrm{H}}\circ(\boldsymbol{H}_l^{\mathrm{H}}\boldsymbol{H}_l)^{\mathrm{T}})\boldsymbol{\psi}^{\mathrm{T}}+\sigma^2}\geq\Gamma_l\\ &\mathrm{tr}\left(\left(\left(\frac{1}{\Gamma_l}+1\right)\boldsymbol{V}_l-\boldsymbol{V}_l^R\right)\boldsymbol{\Xi}\right)\geq\sigma^2,\end{aligned} \tag{56}$$

where

$$\boldsymbol{V}_l=\ \boldsymbol{Q}\boldsymbol{R}_l\boldsymbol{Q}^{\mathrm{H}}\circ(\boldsymbol{H}_l^{\mathrm{H}}\boldsymbol{H}_l)^{\mathrm{T}}, \tag{57}$$

$$\boldsymbol{V}_l^R=\ \boldsymbol{Q}\boldsymbol{R}\boldsymbol{Q}^{\mathrm{H}}\circ(\boldsymbol{H}_l^{\mathrm{H}}\boldsymbol{H}_l)^{\mathrm{T}}. \tag{58}$$

Therefore, the proof of Proposition 2 is completed.

Appendix C
Proof of Proposition 3

To obtain a lower bound for the maximum beampattern gain, we consider the case where the number of feeds is 1, and the analog beamformer at the RHS is derived using the holographic method proposed in [23]. The holographic method provides a closed-form expression to calculate the analog beamforming vector given the direction of the main lobe when the number of quantization bits is $N_b\to\infty$. Assume that the feed is located at the origin, and the spacing between the nearby elements is d_s. To generate a beampattern with a main lobe towards the direction θ_0, the radiated amplitude of the m-th element, based on the method proposed in [23], is

$$\begin{aligned}\psi_m=&\ \frac{1}{2}+\frac{1}{2}\cos(\boldsymbol{k}_m^1(\boldsymbol{r}_m^e-\boldsymbol{r}_1^f)+\boldsymbol{k}_f(\theta_0)\boldsymbol{r}_m^e)\\ =&\ \frac{1}{2}+\frac{1}{4}\left(e^{j\frac{2\pi}{\lambda}(m-1)d_s(n_s+\sin\theta_0)}+e^{-j\frac{2\pi}{\lambda}(m-1)d_s(n_s+\sin\theta_0)}\right),\end{aligned} \tag{59}$$

where $\boldsymbol{k}_m^1$ is the propagation vector of the reference wave emitted from the 1-st feed to the m-th element, $\boldsymbol{r}_m^e$ is the location of the m-th element, and $\boldsymbol{k}_f(\theta_0)$ is the propagation vector in free space with direction θ_0.

Assume that the signal emitted by the feed is x_1, and the reference signal at the location of the m-th element is:

$$x_m^r=x_1\exp\left(-j\frac{2\pi n_s}{\lambda}(m-1)d_s\right), \tag{60}$$

where n_s is the refractive index of the substrate, and λ is the wavelength of the reference wave in free space. Also, the steering vector of the metamaterial elements towards the direction θ can be expressed as:

$$\begin{aligned}\boldsymbol{a}^{\mathrm{T}}(\theta)=&\ \left(1,\cdots,\exp\left(-j\frac{2\pi}{\lambda}(m-1)d_s\sin\theta\right),\cdots,\right.\\ &\left.\exp\left(-j\frac{2\pi}{\lambda}(M-1)d_s\sin\theta\right)\right).\end{aligned} \tag{61}$$

Based on (59), (60), and (61), the signal towards the direction θ is

$$z(\theta)=\sum_{m=1}^{M}a_m(\theta)\psi_m x_m^r$$

$$= \frac{x_1}{2}\sum_{m=1}^{M} e^{-j\frac{2\pi}{\lambda}(m-1)d_s(n_s+\sin\theta)} + \frac{x_1}{4}\sum_{m=1}^{M} e^{-j\frac{2\pi}{\lambda}(m-1)d_s(\sin\theta-\sin\theta_0)} + \frac{x_1}{4}\sum_{m=1}^{M} e^{-j\frac{2\pi}{\lambda}(m-1)d_s(2n_s+\sin\theta+\sin\theta_0)}$$
$$= \frac{x_1}{2}\cdot\frac{\sin\frac{M}{2}f_1(\theta)}{\sin\frac{1}{2}f_1(\theta)}e^{j\frac{M-1}{2}f_1(\theta)} + \frac{x_1}{4}\cdot\frac{\sin\frac{M}{2}f_2(\theta,\theta_0)}{\sin\frac{1}{2}f_2(\theta,\theta_0)}e^{j\frac{M-1}{2}f_2(\theta,\theta_0)} + \frac{x_1}{4}\cdot\frac{\sin\frac{M}{2}f_3(\theta,\theta_0)}{\sin\frac{1}{2}f_3(\theta,\theta_0)}e^{j\frac{M-1}{2}f_3(\theta,\theta_0)}, \quad (62)$$

where $f_1(\theta) = \frac{2\pi}{\lambda}d_s(n_s+\sin\theta)$, $f_2(\theta,\theta_0) = \frac{2\pi}{\lambda}d_s(\sin\theta - \sin\theta_0)$, and $f_3(\theta,\theta_0) = \frac{2\pi}{\lambda}d_s(2n_s+\sin\theta+\sin\theta_0)$. If $\theta=\theta_0$ and $n_s>1$, we have $f_2(\theta,\theta_0)=0$, while $f_1(\theta), f_3(\theta,\theta_0)\neq 0$. Consequently, we have:

$$\lim_{M\to\infty}\left|\frac{x_1}{2}\cdot\frac{\sin\frac{M}{2}f_1(\theta)}{\sin\frac{1}{2}f_1(\theta)}e^{j\frac{M-1}{2}f_1(\theta)}\right| = O(M), \quad (63)$$

$$\lim_{M\to\infty}\left|\frac{x_1}{4}\cdot\frac{\sin\frac{M}{2}f_2(\theta_0,\theta_0)}{\sin\frac{1}{2}f_2(\theta_0,\theta_0)}e^{j\frac{M-1}{2}f_2(\theta_0,\theta_0)}\right| = \frac{x_1M}{4}, \quad (64)$$

$$\lim_{M\to\infty}\left|\frac{x_1}{4}\cdot\frac{\sin\frac{M}{2}f_3(\theta_0,\theta_0)}{\sin\frac{1}{2}f_3(\theta_0,\theta_0)}e^{j\frac{M-1}{2}f_3(\theta_0,\theta_0)}\right| = O(M), \quad (65)$$

which implies $\lim_{M\to\infty}|z(\theta_0)| = x_1M/4$.

Besides, the total power transmitted by the RHS can be expressed as:

$$P_T = \sum_{m=1}^{M}(a_m(\theta)\psi_m x_m^r)\cdot(a_m(\theta)\psi_m x_m^r)^* = \frac{x_1^2}{16}\sum_{m=1}^{M}\left(2+e^{j\frac{2\pi}{\lambda}(m-1)d_s(n_s+\sin\theta_0)}+e^{-j\frac{2\pi}{\lambda}(m-1)d_s(n_s+\sin\theta_0)}\right)^2 \quad (66)$$

Similar to the proof of $\lim_{M\to\infty}|z(\theta_0)| = x_1M/4$, we have:

$$\lim_{M\to\infty} P_T = \frac{3x_1^2M}{8}. \quad (67)$$

To satisfy the sum-power constraint, the total transmit power P_T needs to be P_M, leading to $|x_1| = \sqrt{\frac{8P_M}{3M}}$. Thus, the beampattern gain can be expressed as:

$$\lim_{M\to\infty} P_R(\theta) = \lim_{M\to\infty}|z(\theta_0)|^2 = \frac{P_MM}{6}. \quad (68)$$

Therefore, the proof of Proposition 3 is completed.

Appendix D
Proof of Proposition 4

According to (17), we have:

$$P(\theta,\phi) = (\boldsymbol{a}^{\mathrm{T}}(\theta,\phi)\boldsymbol{\Psi}\boldsymbol{Q}\boldsymbol{B})(\boldsymbol{a}^{\mathrm{T}}(\theta,\phi)\boldsymbol{\Psi}\boldsymbol{Q}\boldsymbol{B})^{\mathrm{H}} \geq 0. \quad (69)$$

Moreover, based on the sum-power constraint (21d), we have:

$$\mathrm{tr}\left(\boldsymbol{\Psi}\boldsymbol{Q}\boldsymbol{B}\boldsymbol{B}^{\mathrm{H}}\boldsymbol{Q}^{\mathrm{H}}\boldsymbol{\Psi}^{\mathrm{H}}\right) = \mathrm{tr}(\boldsymbol{Y}\boldsymbol{Y}^{\mathrm{H}}) = \sum_{i=1}^{M}\sum_{j=1}^{M}|y_{i,j}|^2 = P_M, \quad (70)$$

where $\boldsymbol{Y} = \boldsymbol{\Psi}\boldsymbol{Q}\boldsymbol{B}$. This indicates that $|y_{i,j}| \leq \sqrt{P_M}, \forall i,j$. Thus, we have:

$$P(\theta,\phi) = \sum_{j=1}^{M}\left(\sum_{i=1}^{M}a_i(\theta,\phi)y_{i,j}\right)^2 < M\sum_{j=1}^{M}\sum_{i=1}^{M}(a_i(\theta,\phi)y_{i,j})^2 < MNP_M. \quad (71)$$

As for the first term in the objective function (21a), we have:

$$0 \leq \frac{1}{D}\sum_{d=1}^{D}P(\theta_d,\phi_d) \leq MP_M. \quad (72)$$

As for the cross-correlation between the directions (θ,ϕ) and (θ',ϕ'), we have:

$$|P^c(\theta,\phi,\theta',\phi')| \geq 0 \quad (73)$$
$$|P^c(\theta,\phi,\theta',\phi')| \leq \max\{P(\theta,\phi),P(\theta',\phi')\} \leq MP_M. \quad (74)$$

Thus, the second term of the objective function (21a) satisfies:

$$0 \leq \rho RMSC \leq \rho MP_M. \quad (75)$$

Based on (72) and (75), the lower and upper bounds of the objective function (21a) are:

$$-\rho MP_M \leq \frac{1}{D}\sum_{d=1}^{D}P(\theta_d,\phi_d) - \rho RMSC \leq MP_M. \quad (76)$$

Therefore, the proof of Proposition 4 is completed.

References

[1] M. Di Renzo, M. Debbah, D.-T. Phan-Huy, A. Zappone, M.-S. Alouini, C. Yuen, V. Sciancalepore, G. C. Alexandropoulos, J. Hoydis, H. Gacanin, J. de Rosny, A. Bounceu, G. Lerosey, and M. Fink, "Smart radio environments empowered by ai reconfigurable meta-surfaces: An idea whose time has come," *EURASIP J. Wirel. Commun. Netw.*, no. 129, pp. 1–20, May 2019.

[2] C. Huang, S. Hu, G. C. Alexandropoulos, A. Zappone, C. Yuen, R. Zhang, M. Di Renzo, and M. Debbah, "Holographic MIMO surfaces for 6G wireless networks: Opportunities, challenges, and trends," *IEEE Wirel. Commun.*, vol. 27, no. 5, pp. 118–125, Oct. 2020.

[3] A. Hassanien, M. G. Amin, E. Aboutanios, and B. Himed, "Dual-function radar communication systems: A solution to the spectrum congestion problem," *IEEE Signal Process. Mag.*, vol. 36, no. 5, pp. 115–126, Sept. 2019.

[4] H. Hua, J. Xu, and T. X. Han, "Optimal transmit beamforming for integrated sensing and communication," *arXiv preprint arXiv:2104.11871*, 2021.

[5] D. Ma, N. Shlezinger, T. Huang, Y. Liu, and Y. C. Eldar, "Joint radar-communications strategies for autonomous vehicles combining two key automotive technologies," *IEEE Signal Process. Mag.*, vol. 37, no. 4, pp. 85–97, July 2020.

[6] S. Buzzi, C. D'Andrea, and M. Lops, "Using massive MIMO arrays for joint communication and sensing," in *Proc. 53rd Asilomar Conf. Signals Syst. Comput.*, Pacific Grove, CA, Nov. 2019.

[7] X. Wang, A. Hassanien, and M. G. Amin, "Sparse transmit array design for dual-function radar communications by antenna selection," *Digit. Signal Process.*, vol. 83, pp. 223–234, Dec. 2018.

[8] L. Zheng, M. Lops, Y. C. Eldar, and X.Wang, "Radar and communication co-existence: An overview," *IEEE Signal Process.*, vol. 36, no. 5, pp. 85–89, Sept. 2019.

[9] Z. Feng, Z. Fang, Z. Wei, X. Chen, Z. Quan, and D. Ji, "Joint radar and communication: A survey," *China Commun.*, vol. 17, no. 1, pp. 1–27, Jan. 2020.

[10] J. Moghaddasi and K. Wu, "Multifunctional transceiver for future radar sensing and radio communicating data-fusion platform," *IEEE Access*, vol. 4, pp. 818–838, Feb. 2016.

[11] C. Sturm, T. Zwick, and W. Wiesbeck, "An OFDM system concept for joint radar and communications operations," in *Proc. IEEE 69th Veh. Technol. Conf.*, Barcelona, Spain, Apr. 2009.

[12] F. Liu, L. Zhou, C. Masouros, A. Li, W. Luo, and A. Petropulu, "Toward dual-functional radar-communication systems: Optimal waveform design," *IEEE Trans. Signal Process.*, vol. 66, no. 16, pp. 4264–4279, Aug. 2018.

[13] X. Liu, T. Huang, N. Shlezinger, Y. Liu, J. Zhou, and Y. C. Eldar, "Joint transmit beamforming for multiuser MIMO communications and MIMO radar," *IEEE Trans. Signal Process.*, vol. 68, pp. 3929–3944, June 2020.

[14] F. Liu and C. Masouros, "Hybrid beamforming with sub-arrayed MIMO radar: Enabling joint sensing and communication at mmwave band," in *Proc. IEEE Int. Conf. Acoust. Speech Signal Process. (ICASSP)*, Brighton, UK, Apr. 2019.

[15] Z. Wan, Z. Gao, F. Gao, M. Di Renzo, and M.-S. Alouini, "Terahertz massive mimo with holographic reconfigurable intelligent surfaces," *IEEE Trans. Commun.*, vol. 69, no. 7, pp. 4732–4750, Mar. 2021.

[16] G. Gradoni and M. Di Renzo, "End-to-end mutual coupling aware communication model for reconfigurable intelligent surfaces: An electromagnetic-compliant approach based on mutual impedances," *IEEE Wireless Communications Letters*, vol. 10, no. 5, pp. 938–942, May 2021.

[17] I. Ahmed, H. Khammari, A. Shahid, A. Musa, K. S. Kim, E. D. Poorter, and I. Moerman, "A survey on hybrid beamforming techniques in 5g: Architecture and system model perspectives," *IEEE Commun. Surveys Tutorials*, vol. 20, no. 4, pp. 3060–3097, June 2018.

[18] F. Sohrabi and W. Yu, "Hybrid digital and analog beamforming design for large-scale antenna arrays," *IEEE J. Sel. Topics Signal Process.*, vol. 10, no. 3, pp. 501–513, Apr. 2016.

[19] O. Yurduseven, D. L. Marks, J. N. Gollub, and D. R. Smith, "Design and analysis of a reconfigurable holographic metasurface aperture for dynamic focusing in the fresnel zone," *IEEE Access*, vol. 5, pp. 15 055–15 065, June 2017.

[20] M. A. ElMossallamy, H. Zhang, L. Song, K. G. Seddik, Z. Han, and G. Y. Li, "Reconfigurable intelligent surfaces for wireless communications: Principles, challenges, and opportunities," *IEEE Trans. Cognitive Commun. Netw.*, vol. 6, no. 3, pp. 990–1002, Sept. 2020.

[21] R. Deng, B. Di, H. Zhang, D. Niyato, Z. Han, H. V. Poor, and L. Song, "Reconfigurable holographic surfaces for future wireless communications," *IEEE Wireless Commun.*, to be published.

[22] B. Che, F. Meng, Y. Lyu, Y. Zhao, and Q. Wu, "Reconfigurable holographic antenna with low sidelobe level based on liquid crystals," *J. Physics D: Appl. Physics*, vol. 53, no. 31, pp. 302–315, May 2020.

[23] D. R. Smith, O. Yurduseven, L. P. Mancera, P. Bowen, and N. B. Kundtz, "Analysis of a waveguide-fed metasurface antenna," *Physical Rev. Applied*, vol. 8, no. 5, p. 054048, Nov. 2017.

[24] P. Staff. Holographic Beam Forming and Phased Arrays. Accessed: Aug. 15, 2021. [Online]. Available: https://pivotalcommware.com/wp-content/uploads/2019/10/HBF-vs-APA-White-Paper-2019.pdf

[25] Kymeta. Metamaterial-Surface Flat-Panel Antenna Technology. Accessed: Aug. 15, 2021. [Online]. Available: https://www.kymetacorp.com/wp-content/uploads/2019/06/Metamaterial-Surface-Antenna-Technology.pdf

[26] R. Deng, B. Di, H. Zhang, Y. Tan, and L. Song, "Reconfigurable holographic surface: Holographic beamforming for metasurface-aided wireless communications," *IEEE Trans. Veh. Technol.*, vol. 70, no. 6, pp. 6255–6259, June 2021.

[27] B. Di, "Reconfigurable holographic metasurface aided wideband OFDM communications against beam squint," *IEEE Trans. Veh. Technol.*, vol. 70, no. 5, pp. 5099–5103, May 2021.

[28] J. Hunt, J. Gollub, T. Driscoll, G. Lipworth, A. Mrozack, M. S. Reynolds, D. J. Brady, and D. R. Smith, "Metamaterial microwave holographic imaging system," *JOSA A*, vol. 31, no. 10, pp. 2109–2119, Oct. 2014.

[29] O. Yurduseven, S. Podilchak, and M. Khalily, "Towards holographic beam-forming metasurface technology for next generation CubeSats," in *Int. Conf. UK-China Emerging Technol.*, Glasgow, UK, Aug 2020.

[30] M. C. Johnson, S. L. Brunton, N. B. Kundtz, and J. N. Kutz, "Sidelobe canceling for reconfigurable holographic metamaterial antenna," *IEEE Trans. Antennas Propag.*, vol. 63, no. 4, pp. 1881–1886, Feb. 2015.

[31] B. Di, H. Zhang, L. Song, Y. Li, Z. Han, and H. V. Poor, "Hybrid beamforming for reconfigurable intelligent surface based multi-user communications: Achievable rates with limited discrete phase shifts," *IEEE J. Select. Areas Commun.*, vol. 38, no. 8, pp. 1809–1822, Aug. 2020.

[32] G. R. Curry, *Radar System Performance Modeling*. Norwood, MA: Artech House, 2005.

[33] A. Hassanien, M. G. Amin, Y. D. Zhang, , and F. Ahmad, "Dual-function radar-communications: Information embedding using sidelobe control and waveform diversity," *IEEE Trans. Signal Process.*, vol. 64, no. 8, pp. 2168–2181, Apr. 2016.

[34] M. Boyarsky, T. Sleasman, M. F. Imani, J. N. Gollub, and D. R. Smith, "Electronically steered metasurface antenna," *Sci. Rep.*, vol. 11, no. 4693, Feb. 2021.

[35] S. W. Golomb and G. Gong, *Signal Design for Good Correlation: For Wireless Communication, Cryptography, and Radar*. Cambridge, U.K.: Cambridge Univ. Press, 2005.

[36] G. Sun, G. Liu, and H. Gu, "Signal analysis and processing for random binary phase coded pulse radar," *J. Syst. Eng.*, vol. 15, no. 4, pp. 520–524, Dec. 2004.

[37] P. Stoica, J. Li, and Y. Xie, "On probing signal design for MIMO radar," *IEEE Trans. Signal Process.*, vol. 55, no. 8, pp. 4151–4161, July 2007.

[38] C. A. Balanis, *Modern Antenna Handbook*. Danvers, MA: John Wiley & Sons, 2008.

[39] J. F. Sturm, "Using SeDuMi 1.02, a Matlab toolbox for optimization over symmetric cones," *Optim. Methods Softw.*, vol. 11, no. 1-4, pp. 625–653, Aug. 1998.

[40] Z. Luo, W. Ma, A. M. So, Y. Ye, and S. Zhang, "Semidefinite relaxation of quadratic optimization problems," *IEEE Signal Process. Mag.*, vol. 27, no. 3, pp. 20–34, Apr. 2010.

[41] A. Simonsson, M. Thurfjell, B. Halvarsson, J. Furuskog, S. Wallin, S. Itoh, H. Murai, D. Kurita, K. Tateishi, A. Harada, and Y. Kishiyama, "Beamforming gain measured on a 5g test-bed," in *Proc. IEEE 85th Veh. Technol. Conf.*, 2017, pp. 1–5.

[42] R. J. Mailloux, *Phased Array Antenna Handbook*. Norwood, MA: Artech House, 2017.

[43] N. Lu, N. Cheng, N. Zhang, X. Shen, J. W. Mark, and F. Bai, "Wi-fi hotspot at signalized intersection: Cost-effectiveness for vehicular internet access," *IEEE Trans. Veh. Technol.*, vol. 65, no. 5, pp. 3506–3518, May 2016.

[44] M. A. Richards, *Fundamentals of Radar Signal Processing*. New York, NY: McGraw-Hill, 2005.

[45] L. Wang, W. Zhu, Y. Zhang, Q. Lian, and J. Tang, "Multi-target detection and adaptive waveform design for cognitive mimo radar," *IEEE Sensors J.*, vol. 18, no. 24, pp. 9962–9970, Dec. 2018.

Haobo Zhang (S'19) received the B.S. degree at School of Electrical Engineering and Computer Science in Peking University in 2019, where he is currently pursuing the PhD degree in signal and information processing. His research interests include metasurface, wireless networks, and optimization theory.

Hongliang Zhang (S'15-M'19) received the B.S. and Ph.D. degrees at the School of Electrical Engineering and Computer Science at Peking University, in 2014 and 2019, respectively. He was a Postdoctoral Fellow in the Electrical and Computer Engineering Department at the University of Houston, Texas. Currently, he is a Postdoctoral Associate in the Department of Electrical and Computer Engineering at Princeton University, New Jersey. His current research interest includes reconfigurable intelligent surfaces, aerial access networks, optimization theory, and game theory. He received the best doctoral thesis award from Chinese Institute of Electronics in 2019. He is an exemplary reviewer for IEEE Transactions on Communications in 2020. He is also the recipient of 2021 IEEE Comsoc Heinrich Hertz Award for Best Communications Letters and 2021 IEEE ComSoc Asia-Pacific Outstanding Paper Award. He has served as a TPC Member for many IEEE conferences, such as Globecom, ICC, and WCNC. He is currently an Editor for IEEE Communications Letters, IET Communications, and Frontiers in Signal Processing. He has also served as a Guest Editor for several journals, such as IEEE Internet of Things Journal, Journal of Communications and Networks, etc.

Boya Di (S'15-M'19) obtained her PhD degree from the Department of Electronics, Peking University, China, in 2019. Prior to that, she received the B.S. degree in electronic engineering from Peking University in 2014. She was a postdoc researcher at Imperial College London and is now an assistant professor at Peking University. Her current research interests include reconfigurable intelligent surfaces, multi-agent systems, edge computing, vehicular networks, and aerial access networks. She received the best doctoral thesis award from China Education Society of Electronics in 2019. She is also the recipient of 2021 IEEE ComSoc Asia-Pacific Outstanding Paper Award. She serves as an associate editor for IEEE Transactions on Vehicular Technology since June 2020. She has also served as a workshop co-chair for IEEE WCNC 2020&2021.

Marco Di Renzo (Fellow, IEEE) received the Laurea (cum laude) and Ph.D. degrees in electrical engineering from the University of L'Aquila, Italy, in 2003 and 2007, respectively, and the Habilitation à Diriger des Recherches (Doctor of Science) degree from University Paris-Sud (now Paris-Saclay University), France, in 2013. Since 2010, he has been with the French National Center for Scientific Research (CNRS), where he is a CNRS Research Director (Professor) with the Laboratory of Signals and Systems (L2S) of Paris-Saclay University – CNRS and CentraleSupelec, Paris, France. In Paris-Saclay University, he serves as the Coordinator of the Communications and Networks Research Area of the Laboratory of Excellence DigiCosme, and as a Member of the Admission and Evaluation Committee of the Ph.D. School on Information and Communication Technologies. He is the Editor-in-Chief of IEEE Communications Letters and a Distinguished Speaker of the IEEE Vehicular Technology Society. In 2017-2020, he was a Distinguished Lecturer of the IEEE Vehicular Technology Society and IEEE Communications Society. He has received several research distinctions, which include the SEE-IEEE Alain Glavieux Award, the IEEE Jack Neubauer Memorial Best Systems Paper Award, the Royal Academy of Engineering Distinguished Visiting Fellowship, the Nokia Foundation Visiting Professorship, the Fulbright Fellowship, and the 2021 EURASIP Journal on Wireless Communications and Networking Best Paper Award. He is a Fellow of the UK Institution of Engineering and Technology (IET), a Fellow of the Asia-Pacific Artificial Intelligence Association (AAIA), an Ordinary Member of the European Academy of Sciences and Arts (EASA), and an Ordinary Member of the Academia Europaea (AE). Also, he is a Highly Cited Researcher.

Zhu Han (S'01–M'04-SM'09-F'14) received the B.S. degree in electronic engineering from Tsinghua University, in 1997, and the M.S. and Ph.D. degrees in electrical and computer engineering from the University of Maryland, College Park, in 1999 and 2003, respectively.

From 2000 to 2002, he was an R&D Engineer of JDSU, Germantown, Maryland. From 2003 to 2006, he was a Research Associate at the University of Maryland. From 2006 to 2008, he was an assistant professor at Boise State University, Idaho. Currently, he is a John and Rebecca Moores Professor in the Electrical and Computer Engineering Department as well as in the Computer Science Department at the University of Houston, Texas. His research interests include wireless resource allocation and management, wireless communications and networking, game theory, big data analysis, security, and smart grid. Dr. Han received an NSF Career Award in 2010, the Fred W. Ellersick Prize of the IEEE Communication Society in 2011, the EURASIP Best Paper Award for the Journal on Advances in Signal Processing in 2015, IEEE Leonard G. Abraham Prize in the field of Communications Systems (best paper award in IEEE JSAC) in 2016, and several best paper awards in IEEE conferences. Dr. Han was an IEEE Communications Society Distinguished Lecturer from 2015-2018, AAAS fellow since 2019 and ACM distinguished Member since 2019. Dr. Han is 1% highly cited researcher since 2017 according to Web of Science. Dr. Han is also the winner of 2021 IEEE Kiyo Tomiyasu Award, for outstanding early to mid-career contributions to technologies holding the promise of innovative applications, with the following citation: "for contributions to game theory and distributed management of autonomous communication networks."

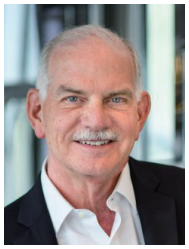

H. Vincent Poor (S'72, M'77, SM'82, F'87) received the Ph.D. degree in EECS from Princeton University in 1977. From 1977 until 1990, he was on the faculty of the University of Illinois at Urbana-Champaign. Since 1990 he has been on the faculty at Princeton, where he is currently the Michael Henry Strater University Professor. During 2006 to 2016, he served as the dean of Princeton's School of Engineering and Applied Science. He has also held visiting appointments at several other universities, including most recently at Berkeley and Cambridge. His research interests are in the areas of information theory, machine learning and network science, and their applications in wireless networks, energy systems and related fields. Among his publications in these areas is the forthcoming book Machine Learning and Wireless Communications. (Cambridge University Press). Dr. Poor is a member of the National Academy of Engineering and the National Academy of Sciences and is a foreign member of the Chinese Academy of Sciences, the Royal Society, and other national and international academies. He received the IEEE Alexander Graham Bell Medal in 2017.

Lingyang Song (S'03–M'06-SM'11-F'19) received his PhD from the University of York, UK, in 2007, where he received the K. M. Stott Prize for excellent research. He worked as a postdoctoral research fellow at the University of Oslo, Norway, and Harvard University, until rejoining Philips Research UK in March 2008. In May 2009, he joined the School of Electronics Engineering and Computer Science, Peking University, China, as a full professor. His main research interests include cooperative and cognitive communications, physical layer security, and wireless ad hoc/sensor networks. He published extensively, wrote 6 text books, and is co-inventor of a number of patents (standard contributions). He received 9 paper awards in IEEE journal and conferences including IEEE JSAC 2016, IEEE WCNC 2012, ICC 2014, Globecom 2014, ICC 2015, etc. He is currently on the Editorial Board of IEEE Transactions on Wireless Communications and Journal of Network and Computer Applications. He served as the TPC co-chairs for the International Conference on Ubiquitous and Future Networks (ICUFN2011/2012), symposium co-chairs in the International Wireless Communications and Mobile Computing Conference (IWCMC 2009/2010), IEEE International Conference on Communication Technology (ICCT2011), and IEEE International Conference on Communications (ICC 2014, 2015). He is the recipient of 2012 IEEE Asia Pacific (AP) Young Researcher Award. Dr. Song is a fellow of IEEE, and IEEE ComSoc distinguished lecturer since 2015.